Available online at www.sciencedirect.com

ScienceDirect

journal homepage: www.elsevier.com/locate/he

Impact of strontium non-stoichiometry of $Sr_xTi_{0.3}Fe_{0.7}O_{3-\delta}$ on structural, electrical, and electrochemical properties for potential oxygen electrode of intermediate temperature solid oxide cells

Aleksander Mroziński [a,*], *Sebastian Molin* [a], *Patryk Błaszczak* [b], *Tadeusz Miruszewski* [b], *Karolina Górnicka* [b], *Jakub Karczewski* [b], *Piotr Jasiński* [a]

[a] *Faculty of Electronics, Telecommunications and Informatics and Advanced Materials Center, Gdańsk University of Technology, ul. G. Narutowicza 11/12, 80- 233 Gdańsk, Poland*

[b] *Faculty of Applied Physics and Mathematics and Advanced Materials Center, Gdańsk University of Technology, ul. G. Narutowicza 11/12, 80- 233 Gdańsk, Poland*

HIGHLIGHTS

- Knowledge about the influence of A site non-stoichiometry in STF has been extended.
- The electrochemical characterisation was performed on symmetrical and full cells.
- The DRT technique allowed to distinguish the dominant electrochemical process.
- The non-stoichiometric STF shows improved electrochemical properties.

GRAPHICAL ABSTRACT

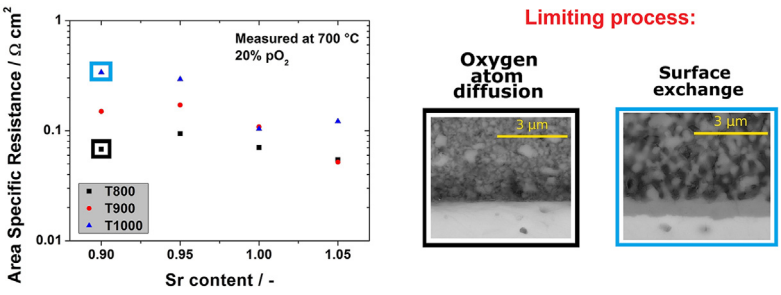

ARTICLE INFO

Article history:
Received 31 March 2023
Received in revised form
14 May 2023
Accepted 29 May 2023
Available online 14 June 2023

ABSTRACT

This work presents the results of a comprehensive study on the impact of the A-site non-stoichiometry of $Sr_xTi_{0.3}Fe_{0.7}O_{3-\delta}$ (x = 0.90, 0.95, 1.00, 1.05) ceramics on their physicochemical properties. The materials were fabricated by the conventional solid-state reaction method and their structure was determined by X-ray diffractometry, X-ray photoelectron spectroscopy and electron microscopy. Their sintering and thermal expansion properties were then evaluated. The electrical properties of the materials were determined by electrical conductivity and electrical relaxation measurements (on bulk materials) and by

* *Corresponding author.*
E-mail address: aleksander.mrozinski@pg.edu.pl (A. Mroziński).

https://doi.org/10.1016/j.ijhydene.2023.05.323

Keywords:
Perovskite
Oxygen electrode
Strontium non-stoichiometry
Distribution of relaxation times
Solid oxide cells

electrochemical impedance spectroscopy (EIS) studies of symmetrical, CGO-electrolyte based, porous electrodes. Finally, fuel cell tests with the non-stoichiometric electrodes were evaluated. To elucidate the electrochemical reaction pathways for oxygen reduction/evolution reaction, EIS measurements were carried out in different pO_2 and were analysed via the distribution of relaxation times method. The results showed a dependence of materials' properties on the A-site non-stoichiometry, which can be used to fine-tune their properties, e.g. increase the surface exchange rate or decrease the thermal expansion coefficient.

Introduction

Solid Oxide Cells (SOCs) are energy conversion devices that can be used for energy generation (SOFCs – Solid Oxide Fuel Cells) and storage (by utilising SOECs – Solid Oxide Electrolysis Cells) [1]. Unfortunately, the performance of SOCs is limited by the electrochemical reactions at the electrodes [2–4], including the oxygen reduction/evolution reaction rate at intermediate temperatures (<700 °C) [5–7]. Therefore, improved and new electrode materials are sought [8–14]. Perovskite oxides (general formula ABO_3) with mixed ionic and electronic conductivity (MIEC) are perspective materials for SOFC electrodes [15–21], which allow for a wide range of compositional tailoring and fine-tuning of their structural and chemical properties. Historically, the most active oxygen electrodes contain Co, which providies high electrochemical activity due to its mixed valence [22–27]. Recent years have however highlighted Co as a problematic material due to its cost and unsustainable mining. Doped strontium titanates seem an interesting Co-free alternative material [28–30]. Doped strontium titanates have been used as oxygen membranes [31,32], resistive random access memory [33], oxygen sensors [34,35], coatings for porous stainless steel [36], fast electronic devices [37,38], quantum devises [39], and electrodes in SOFCs [40–43].

Previous research on the oxygen reduction reaction (ORR) on doped $SrTiO_3$ has focussed on materials with substitution at the A or/and B sublattices [44–49]. For example, Zhang et al. reported excellent electrochemical properties at 700 °C (polarisation resistance 0.043 Ω cm^2) for $SrTiO_3$ substituted at both sublattices, despite much lower electrical conductivity than the conductivity of $La_{0.6}Sr_{0.4}Co_{0.2}Fe_{0.8}O_{3-\delta}$ (~20 S cm^{-1} and ~300 S cm^{-1}, respectively) [43,50].

One of the options for improving perovskite materials is increasing the oxygen vacancies by introducing a non-stoichiometry at the A or B site [51–54]. Several works studying the influence of A-site or B-site deficiency on the properties of doped strontium titanate oxygen electrodes have been published. Ni et al. [55,56] investigated $Sr_{1-x}Ti_{0.3}Fe_{0.6}Ni_{0.1}O_3$ (x = 0, 0.02, 0.05) as an oxygen electrode at 750 °C. They have indicated that Sr deficiency promotes better electrochemical properties because of a higher amount of oxygen vacancies and a smaller thermal expansion coefficient (TEC). The best results in terms of electrochemical performance were obtained for the material with x = 0.05 despite a slight decrease of conductivity. Further research was carried out by Ni et al. [17], who improved the electrochemical properties of $Sr_{0.95}Ti_{0.3}Fe_{0.6}Ni_{0.1}O_3$ by exsolution of (Ni,Fe)O nanoparticles. Zhu et al. proved that the exsoluted $Sr_{0.95}(Ti_{0.3}Fe_{0.63}Ni_{0.07})O_{3-\delta}$ anode has better electrochemical performance than stoichiometric material in the range 700 °C–850 °C. Shan and Guo's [57] research on a $(Y_{0.08}Sr_{0.92})_{1-x}Ti_{0.6}Fe_{0.4}O_{3-d}$ mixed conductor showed a decrease in conductivity when the A-site deficiency increased. Similar behaviour of conductivity was reported for $Sr_{1-x}Fe_{0.8}Ti_{0.2}O_{3-\delta}$ by Kharton et al. [58] and for $Sr_xFe_{0.7}Ti_{0.3}O_{3-\delta}$ by Yang et al. [59]. Opposite behaviour of conductivity was observed by Li et al. for $Sr(Ti_{0.6}Fe_{0.4})_{1-x}O_{3-\delta}$ where B-site deficiency was implemented [60]. Despite the above-mentioned literature reports on non-stoichiometric doped strontium titanates, the influence of the physical and chemical properties of non-stoichiometric materials on the electrochemical performance and electrochemical processes has not been shown.

In our previous work we have identified $SrFe_{0.7}Ti_{0.3}O_{3-\delta}$ as an active catalyst [61]. Therefore, in this work, we study of $Sr_xFe_{0.7}Ti_{0.3}O_{3-\delta}$ (STF-x) with x = 0.90; 0.95; 1.00; 1.05. We report the fundamental material analysis including X-ray diffraction (XRD), particle size distribution (PSD), powder specific surface area (SSA), thermogravimetric analysis (TGA), linear thermal expansion, X-ray photoelectron spectroscopy (XPS), H_2-Thermally Programmed Reduction/Desorption (H_2-TPR/TPD) of STF-x powder and the results of total electrical conductivity and conductivity relaxation of STF-x pellets. Finally, an electrochemical impedance spectroscopy (EIS) study, including a distribution of relaxation times (DRT) analysis, of symmetrical cells under SOC operating conditions and different oxygen partial pressures are demonstrated.

Experimental

Materials synthesis

Stoichiometric $Sr_{1.00}Ti_{0.3}Fe_{0.7}O_{3-\delta}$ (STF-100) and non-stoichiometric $Sr_{0.90}Ti_{0.3}Fe_{0.7}O_{3-\delta}$ (STF-90), $Sr_{0.95}Ti_{0.3}Fe_{0.7}O_{3-\delta}$ (STF-95), and $Sr_{1.05}Ti_{0.3}Fe_{0.7}O_{3-\delta}$ (STF-105) powders were synthesised using the conventional solid state reaction method. Starting reagents: $SrCO_3$ (EuroChem, Poland), TiO_2 (EuroChem, Poland) and Fe_2O_3 (Chempur, Poland) were mixed in a planetary ball mill (Fritsch, Pulverisette 7) for 12 h. All starting powders were >99.9% pure. The mixed reagent

powders of STF-100 and STF-105 (in the form of pellets) were sintered two times at 1200 °C (for 15 h each time) with an intermediate grinding step between the sinterings. Due to the higher sinterability of strontium-deficient compounds, the synthesis temperature was decreased to 1100 °C for the STF-90 and STF-95. After sintering, STF-x pellets were reground in a mortar and milled in two stages in a planetary ball mill. Firstly, using 3 mm YSZ balls and a rotational speed of 1000 rpm for 1 h and next using 1 mm ZrO_2 balls and 1100 rpm, also for 1 h. Finally, the milled STF-x powders were thermally relaxed at 600 °C as described earlier [62].

Sample preparations

For the electrical conductivity and electrical conductivity relaxation measurements, the synthesised STF-x powders were uniaxially pressed and sintered for 2 h at the same temperature as during synthesis. The achieved pellets were ~1 mm in thickness and ~12 mm in diameter. For the electrical conductivity relaxation studies, pellets were also cut into the shapes of a prisms (12 × 1 mm x 2 mm) using a precision tungsten wire saw.

Porous STF-x electrodes for electrochemical impedance spectroscopy of symmetrical cells were applied on a dense gadolinium-doped ceria (CGO-20, $Ce_{0.8}Gd_{0.2}O_{2-\delta}$) substrate. Commercially available CGO-20 (DKK, Japan) powders were pressed into pellets and sintered at 1400 °C for 8 h. The sintered disks had a diameter of 13 mm and 98% theoretical density. The CGO-20 pellets were polished down to a 3 μm finish and a thickness of 0.6 mm ± 10%. For the application of the STF-x materials on the CGO-20 substrates, the synthesised powders were mixed with a commercial vehicle (Heraeus, V-006 A) at a weight ratio of 2:3 using a planetary ball mill. The STF-x pastes were screen-printed on two sides of the CGO-20. Each side received two layers with a drying step at 130 °C after each application. Symmetrical samples were sintered at 800 °C, 900 °C and 1000 °C for 2 h under an air atmosphere. The produced electrodes had an active surface area equal to 0.5 cm^2 and ~20 μm thickness. As in our previous work, platinum was used as a current collector [61].

For application tests in a SOFC system, selected STF-x (x = 0.95 and 1.05) materials were also screen printed on commercial Elcogen button half cells (ACS-400B) and sintered at 800 °C and 1000 °C, respectively. Finally, for comparison, a reference SOFC with commercially available, state-of-the-art LSCF cathode material (ESL Europe) was sintered at 1050 °C (for 2 h).

Material characterisations

The phase composition of the STF-x powders was characterised by the X-ray diffraction (XRD) technique. Measurements were carried out at room temperature in air using a Bruker D2 Phaser with an XE-T detector equipped with a Cu X-ray anode.

X-ray Photoelectron Spectroscopy analysis (XPS) was performed using an Omicron NanoTechnology X-ray photoelectron spectrometer with a 128-channel collector. The XPS measurements were performed under ultra-high vacuum conditions. Photoelectrons were excited by an Mg-Kα X-ray source with an X-ray anode operated at 15 keV and 300 W. The spectra were deconvoluted using the XPSPEAK software.

The H_2-TPR (temperature programmed reduction) was performed using an apparatus equipped with a TCD detector (Buck Scientific, USA), cold trap, and heated gas transfer line. 100 mg of sample powder was placed in a quartz reactor with an internal measurements of the bed temperature. The STF-x powders were degassed at 200 °C for 20 min in a stream of He prior to the measurements. The samples were reduced under the flow of a 40 ml min^{-1} 5% H_2/Ar gas mixture. The tests were performed up to 900 °C with a heating rate of 10 °C min^{-1}.

O_2-TPD (temperature programmed desorption) was performed using 250 mg of prepared powdered sample with the preparation step as described for the H_2-TPR experiment. After the degassing step and cooling down to 50 °C, the quartz reactor was flushed with pure 4N5 O_2 (40 ml min^{-1}) for 1 h. After that, the gas was switched back to He for 1 h in order to equilibrate. The O_2-TPD was performed up to 900 °C with a heating rate of 10 °C min^{-1}. The profiles were collected using the PeakSimple software with a resolution of 1 Hz.

The specific surface area (SSA) was measured and calculated according to the BET isotherm model using a NovaTouch LX1 physisorption apparatus (Quantachrome, USA). The powder samples were degassed at 300 °C for 3 h under a vacuum prior to the measurement.

The particle size distributions of the powders were obtained using a Zetasizer Nano dynamic light scattering analyser (Malvern Panalytica). Measurements of the STF-x solution in ethanol using backscattering mode (detection angle was 173°) were performed at room temperature after a 20 min ultrasound bath.

The kinetics of the thermal decomposition of the STF-x powders were evaluated using thermogravimetric analysis (TGA). The TGA experiments were carried out using a microbalance (CI Precision MK5) in the temperature range between 900 °C and 200 °C. During the whole measurement procedure, air was fed to the furnace chamber at a flow rate of 40 ml min^{-1}. No baseline correction was made for the change in atmosphere density during heating.

Linear thermal expansion results for the STF-x powders were obtained with a Netzsch DIL 402. Pressed powers in form of cylinder were placed in measuring chamber. The samples were heated up to 1100 °C at a heating rate of 5 °C min^{-1}, and after 15 min of dwelling, were cooled down to room temperature at the rate of 3 °C min^{-1} (all in Synthetic Air).

Electrical and electrochemical performance analysis

DC electrical conductivity measurements of the STF-x pellets between 900 °C and 200 °C, were performed using the van der Pauw technique, as described in previous work [61]. The pellets were ~12 mm in diameter and ~1 mm thick. The conductivity was measured in 20% O_2, 5% O_2 and 1% O_2. Synthetic air was used as the base gas, which was further diluted with 5 N Ar using Brooks thermal mass flow controllers to obtain lower pO_2.

To specify the chemical oxygen surface exchange coefficient (k*) and chemical diffusion coefficient of oxygen (D*), the

electrical conductivity relaxation (ECR) technique was used [63]. Studies were performed in a small tube furnace (internal diameter ~20 mm) with 64 cm^3 gas volume. The applied temperatures were 800 °C, 750 °C, 700 °C, 650 °C, and 600 °C. During the four-point single frequency electrochemical impedance spectroscopy measurement (1 Hz), the oxygen partial pressures were changed from 20% O_2 to 10% O_2 and the reverse. The impedance was logged every 5 s until sample stabilisation. The gas flow was constant during the measurement (80 ml min^{-1}). After converting the recorded impedance to conductivity (σ), the results were analysed using the ECR-TOOLS software [64].

For electrochemical impedance spectroscopy (EIS) measurements, a Novocontrol Alpha-A with a ZG-4 interface was used. Symmetrical cells were tested in a 4-wire compression cell placed inside a sealed quartz tube. All measurements were at 25 mV amplitude with a frequency range varying from 3 MHz to 0.05 Hz. In the case of the STF-x electrodes sintered at different temperatures evaluated by impedance spectroscopy, each sample was measured in synthetic air between 800 °C and 500 °C. Samples for the selected sintering temperature were tested at 700 °C under a controlled oxygen concentration (100%, 50%, 20%, 10%, 5%, 2.5%, 1%). Appropriate gas mixtures were achieved using a Brooks thermal mass flow controller.

Characterisation of the fuel cells was performed on an Open Flanges™ test setup by Fiaxell. The anode of the tested fuel cell was electrically connected by a nickel mesh. An Au mesh was used to connect the cathode side. A thin layer of LSC (Fiaxell ink paste) was brush painted on all cathodes (STF-x and LSCF) before the test and dried at 70 °C to improve current collection. Alumina felt was used to separate the gases. The Fiaxell setup was placed inside a Kittec temperature controller furnace. The fuel cells were heated up to 750 °C (3 °C min^{-1}) for reduction and then cooled down to 700 °C for the main test after 24 h stabilisation. Reduction of the anode was conducted in H_2 with 3 vol% of steam, while on the cathode side, synthetic air was applied as the oxidant. Electrochemical impedance spectroscopy (at OCV and 3 vol% of steam) and current–voltage plots were measured by a Solartron 1260/1287 frequency analyser. EIS tests with a controlled oxygen concentration (3%, 5%, 10%, 20%, 50%) were performed with 50 vol% of steam. Appropriate oxygen concentration (cathode side) and steam content (anode side) were achieved using a Brooks thermal mass flow controller. High steam content was obtained by mixing hydrogen and oxygen in an external tubular furnace (700 °C) containing a platinum catalyst. All fuel cell tests were conducted with the total flow rates of 100 ml min^{-1} and 200 ml min^{-1} on anode and cathode side, respectively.

In order to designate the Area Specific Resistance (ASR) collected EIS spectra (polarisation resistance) were recalculated for the area of the electrode (0.5 cm^2) and divided by two as the interfaces were identical. Each impedance spectrum was corrected for the inductance of the rig. The data was analysed by the DRTTOOLS software [65] in the same manner as earlier [61]. In the case of tests with different oxygen concentrations, the data were also fitted using the Elchemea Analytical web-tool (www.elchemea.com, DTU Energy).

Post-mortem SEM

Images of the polished cross sections (with a 1 μm finish) of the measured symmetrical cells with STF-x porous electrodes sintered at different temperatures and of dense STF-x pellets were taken by an FEI Quanta FEG 250 Scanning Electron Microscope (SEM) with a backscattered electron detector and 20 kV in high vacuum. Chemical composition of polished cross-section of STF-x pellets was determined using the Thermo Fischer Phenom XL microscope with an integrated energy dispersive x-ray spectrometer (EDX).

Results and discussion

Characterisation of $Sr_xTi_{0.3}Fe_{0.7}O_{3-\delta}$ powders and bulk materials

The crystallographic structure of the prepared powders was characterised by X-ray diffractometry (XRD). All investigated $Sr_xTi_{0.3}Fe_{0.7}O_{3-\delta}$ powders revealed a cubic perovskite structure (*Pm-3m*), i.e. the structure remained stable even though altering the A-site occupation. Fig. 1 A) shows that the measured XRD patterns match well with the $SrTiO_3$ cubic lattice obtained from the crystallographic database. What is more stoichiometry of obtained STF-x materials was confirmed by the EDX analysis of sintered pellets (Table S.1). A small peak on XRD patterns related to the $SrCO_3$ phase could be identified (at 2θ ~24°) for STF-100 and STF-105. Due to high reactivity of doped strontium titanates, on the surface of STF-100 and STF-105 small amount of $SrCO_3$ is forming via reaction of terminating SrO crystal planes with CO_2 from the air, what cannot be avoided during the powder preparation, processing, or storage [66]. The presence of the $SrCO_3$ compound is of no surprise and can be easily explained on the basis of the research on the SrO–CO_2–$SrCO_3$ equilibrium system, where the process of the carbonate formation greatly depends on the partial pressure of the CO_2 and the humidity of the atmosphere under which the powder was prepared. Above 900 °C the $SrCO_3$ is favoured to be decomposed into SrO what was confirmed by firing powders at 950 °C for 24 h in synthetic air (Figure S.2). This indicates that under the working conditions of the cell, where there is no obvious availability of the CO_2 in the gas stream, the surficial $SrCO_3$ is most likely being decomposed nearly fully into SrO [67–69].

The unit cell parameters were calculated each time using Rietveld refining method (GOF <1.8) and plotted as a function of the Sr-content in Fig. 1 B). The unit cell size of the stoichiometric STF-100 was 3.8845 (5) Å, which is in very good agreement with the literature data [28,70]. For the STF-90, STF-95 and STF-105 unit cell size equals to 3.8909 (1) Å, 3.8879 (2) Å and 3.8832 (7) Å, respectively. A good, monotonic correlation between the A-site occupation and the unit cell size is observed. Small deviation from linear trend probably is correlated with $SrCO_3$ formation in case of STF-105. Removal of Sr from the STF results in an increasing unit cell size. Sr^{2+} deficiency can be charge-balanced by the removal of oxygen (O^{2-}) from the lattice (the formation of oxygen vacancies) or via oxidation of iron ions. Such a mechanism was observed *i.a.* by Zhao et al. [71] in yttrium-doped strontium titanate with A-

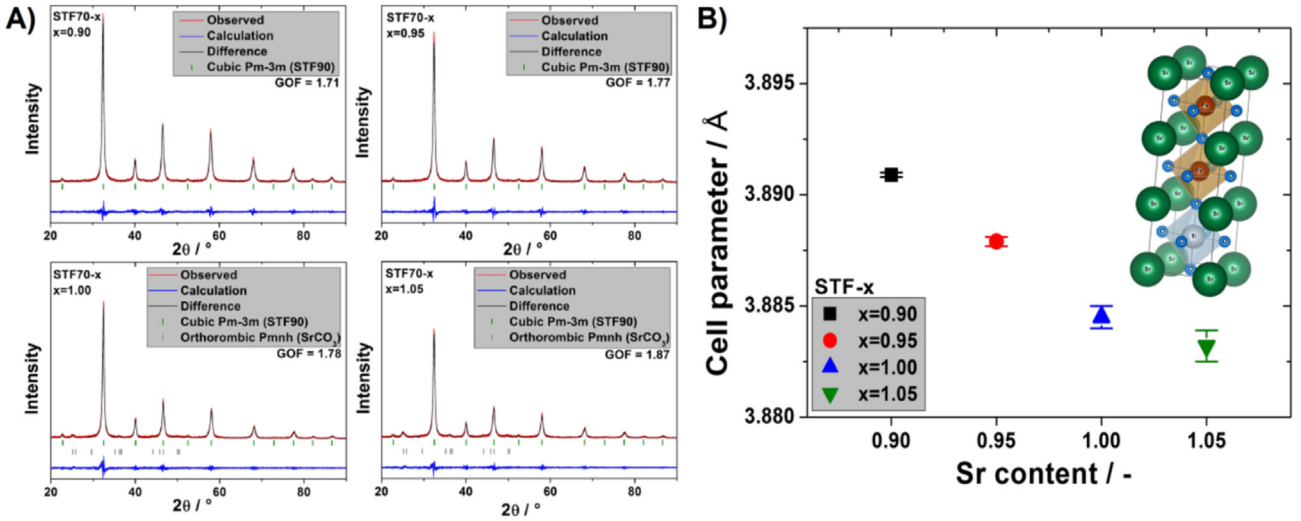

Fig. 1 – X-ray diffractometry spectra of the STF-x powders measured at room temperature (A) and calculated cell parameter value (B).

site deficiency ($(Y_{0.08}Sr_{0.92})_{1-x}TiO_{3-\delta}$). Strontium deficiency in the structure was charge-compensated by both the decrease of Ti^{3+}- ion concentration and the increase of oxygen vacancy concentration. In this work, change of the valence state of iron from 3+ to 4+ induces a large decrease (about 10%) of the ionic radius (0.645 Å vs. 0.585 Å) [72], whereas the observed lattice size change (STF105 vs STF90) is opposite (increase about ~0.2% of the unit cell parameter). Thus the effect of Sr-non-stoichiometry on the lattice must be complex and involve these two compensation mechanisms.

Moreover, the removal of oxygen from the structure and the change in the oxidation state of iron also change the length of the bonds between Fe and O in TiO_6 octahedra. This, in turn, significantly affects the unit cell parameter what was observed in this work. Ward et al. shows that for $Pr_{1-x}Sr_xFeO_{3-\delta}$ with lowering concentration of Sr^{+2} unit cell parameter also increase and with the increase of the oxidation state of iron (smaller ionic radius), Fe–O inter-ion distance leads to lowering of the average Fe–O bonding energy of the redox-active Fe [73]. All facts mentioned above may explain the observed changes in the lattice constant with the changing content of strontium in the structure.

The morphology of the powders was characterised by scanning electron microscopy and particle size measurements, supplemented with specific surface area (SSA) determination.

Fig. 2 A) presents the results of the particle size distribution (PSD) measurements and specific surface area of the STF-x

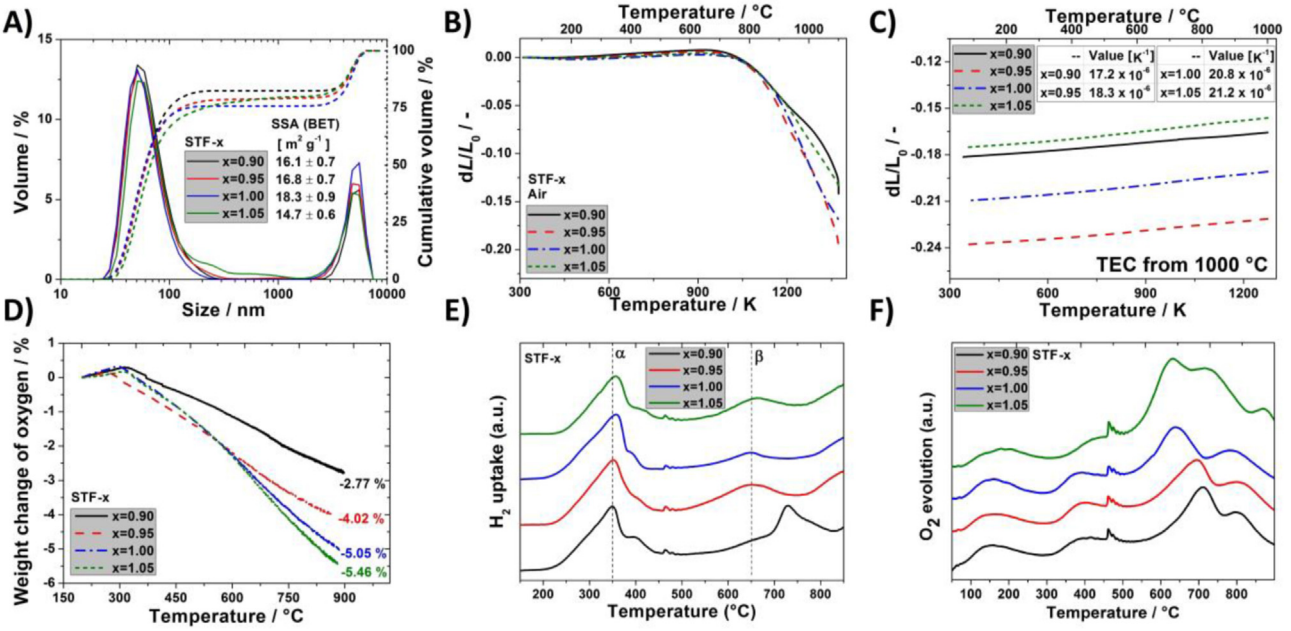

Fig. 2 – Particle size distribution and specific surface area (A), sintering/expansion curves (B–C), thermogravimetric dependence (D), H_2-TPR (E) and O_2-TPD (F) curves for investigated STF-x.

powders. For all cases, similar particle size distributions and specific surface areas (~15 $m^2\ g^{-1}$) were observed, i.e. no clear effect of the A-site occupation on the powders (e.g. particle coarsening, etc.) could be identified. Approximately 75% of the cumulative volume was formed by particles smaller than 100 nm. PSD measurement showed that ~25% of the cumulative volume was formed by larger particles (~5 μm), whilst the SEM examination (Figure S.1) confirmed presence of only relatively small particles. Interestingly, there was no large aggregates found during the SEM imaging, what may suggest that the presence of the larger particles in PSD result may be caused by the apparatus error due to the upper detection limit. The obtained particle size of the powders can be considered small, which may be advantageous for electrochemical reaction for mixed conducting SOC electrodes. For comparison, Schulze-Kuppers et al. reported preparation of $SrTi_{1-y}Fe_yO_{3-\delta}$- materials also including ball milling. In their case, 90% of the particles had a size lower than a few microns with a resulting much smaller specific surface area (~3 $m_2\ g^{-1}$) [74].

The results of the dilatometry measurements conducted in air are presented in Fig. 2 B)–C). The sintering profile for all STF-x materials looks similar to that reported earlier for the $SrTi_{1-y}Fe_yO_{3-\delta}$ materials [62]. For all of the investigated compounds, the onset of sintering is quite similar: from ~760 °C to ~810 °C. The main differences are observed during heating between 800 °C and 1100 °C. The most Sr-deficient sample, STF-90, shows non-linear bahaviour at high temperatures, whereas the STF-95 and STF-100 show similar sintering profiles.

The TEC values for the STF-x were calculated based on the cooling profiles from dilatometry. Obtained values were ~17, ~18–21, and ~21 × $10^{-6}\ K^{-1}$ for STF-90, STF-95, STF-100, and STF-105, respectively. The differences between the TEC values indicate that the STF-x thermal expansion properties are directly related to the strontium content, possibly caused by different chemical expansion contributions due to oxygen release and different amounts of reducible Fe^{4+} ions, which is consistent with the oxygen loss data (Fig. 2 D). The introduction of Sr-nonstoichiometry can be used to reduce the relatively high TEC value of STF-x. Kharton et al. showed comparable TEC values for $Sr_{0.97}Ti_{1-y}Fe_yO_{3-\delta}$ where y > 0.6 [15]. The values are also comparable with data from Zhang et al. although the TEC profiles reported here are linear in the measurement range RT-900 °C, whereas they reported non-linear behaviour [40]. Despite this relatively high TEC value, the STF-x materials can be successfully used as a SOC oxygen electrode, as is in the case of the state-of-the-art materials, e.g. $La_{0.6}Sr_{0.2}Co_{0.2}Fe_{0.8}O_{3-\delta}$ or $La_{0.6}Sr_{0.4}CoO_{3-\delta}$, with TECs>18 × $10^{-6}\ K^{-1}$ [75,76].

To study the temperature-dependent weight loss properties due to oxygen release caused by the thermal reduction of transition metals, thermogravimetric (TG) measurements were carried out between 200 °C and 900 °C in air. Since the changes in powders' mass during TG measurements were related only to the absorption or release of the oxygen, Fig. 2 D) shows only the change of the mass of oxygen contained within the STF-x compounds as a function of temperature. All samples show weight loss on heating, indicative of lattice oxygen release and the formation of oxygen vacancies. Up to 550 °C, the weight loss followed a similar trend for STF-95/100/105, whereas for the STF-90 sample, smaller weight loss was observed. Above 550 °C, after reaching 900 °C, the weight loss was the highest (>5%) for the samples with high Sr content (STF-105 and STF-100). The lowest weight loss was measured for the most Sr-deficient sample (STF-90: ~2.8%). The oxygen release accompanied by oxygen vacancy formation must be charge balanced to preserve electrical neutrality through the reduction of Fe^{4+} to Fe^{3+}.

The determined weight change, presented in Fig. 2 D), has a similar profile to that reported by Zhang et al. The main difference is the temperature of the inflection point. In this work, the inflection points occur at ~300 °C, while for $SrTi_{1-y}Fe_yO_{3-\delta}$, Zhang obtained the inflection at ~400 °C [40].

The H_2-TPR profiles of the STF-x samples are presented in Fig. 2 E). The reduction profiles in all cases contain two main peaks located at around 350 °C (α) and 650 °C (β) except for the STF-90 sample where the secondary β peak is shifted 100 °C towards higher temperatures. Sr and Ti are assumed not to undergo reduction under the used conditions, so the peaks were assigned to Fe-related processes only. The α peak was associated with the reduction of Fe^{4+} to Fe^{3+}, while the β peak located at higher temperatures was related to the reduction of Fe^{3+} to Fe^{2+}. The additional peak at ~720 °C, visible for the STF-90 sample, could be attributed to the simultaneous reduction of created Fe^{2+} to Fe^0 [77,78]. The existence of metallic Fe^0 in the STF-90 compared to the other compounds was also confirmed through the post-mortem XRD measurements (Figure S.3).

The α peak shifts slightly to a higher temperature with the increasing amount of Sr in the A sublattice. Higher amounts of Sr in the lattice stabilise the STF structure, increasing its reduction temperature presenting also an increase in the concentration of lower valence iron ions.

The oxygen desorption measurements (O_2-TPD) revealed quite similar behaviour of the STF-x samples at low temperatures up to ~550 °C, which can be described by the release of chemisorbed oxygen molecules bound loosely to the sorption centres at the surface of the powders (Fig. 2 F). At high temperatures, the peaks were correlated to the evolution of the bulk lattice oxygen [35]. The STF-100 and STF-105 showed faster onset with the peak position of 640 °C, whereas for the STF-95 and STF-90 the peaks were shifted to 700 °C and 710 °C, respectively. The changed look of the O_2-TPD profile of STF-105 sample in the high temperature region most probably corresponds to the evolution of the CO_2 gas from the $SrCO_3$ secondary phase. O_2-TPD measurements indicate that Sr-deficiency results in a lower tendency of the perovskite to release the oxygen from its structure, which is consistent with the TG results, where the Sr-deficient samples showed decreased thermal reducibility.

The surface composition of the STF-x powders was measured using XPS at room temperature under ultra-high vacuum conditions. Deconvolutions of the Fe2p spectra for all samples are presented in Fig. 3 A). Both Fe^{3+} and Fe^{4+} species were identified in all of the synthesised materials. The doublet peak separated by 134 eV located at around 710 eV was assigned to the Fe^{3+} state of iron, whilst the peak situated at ~712.5 eV corresponded to the coexisting Fe^{4+} ions. This behaviour is very characteristic for this type of the compounds based on the Fe-substituted $SrTiO_3$ [55,79]. The

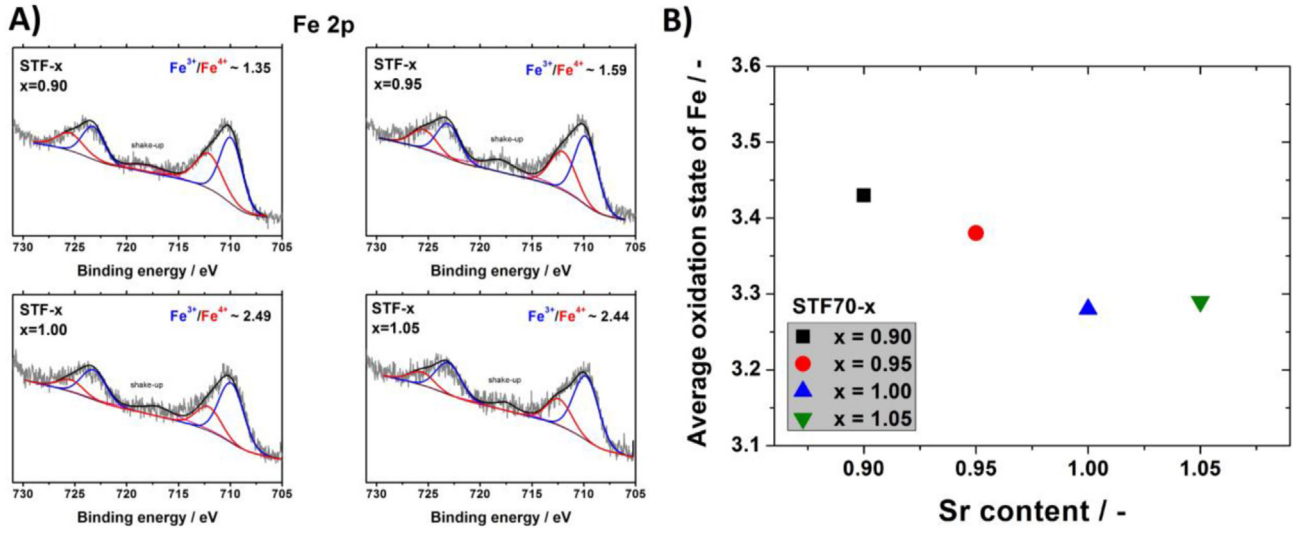

Fig. 3 – Fe 2p spectra (A) and relation of Fe^{+3}/Fe^{+4} ions as a function of Sr content for STF-x powders.

characteristic shake-up lines were also detected, clearly distinguishable mainly for STF-90 and STF-95. It is visible that with the increasing strontium content in the A sublattice, the Fe^{+3}/Fe^{+4} ratio is being elevated. The increase in the Fe mean valence (Fig. 3 B) is considered as one of the mechanism of the charge compensation when A site is being depleted of Sr ions. Despite that the oxygen nonstoichiometry and formation of the oxygen vacancies may have the dominant role, due to the relatively low changes in the increase of the amount of higher valence Fe ions comparing to the removal of the A site cations. Even though the XPS technique surveys just a surface of the materials we can, with high dose of the probability, estimate that similar stoichiometry between Fe^{3+} and Fe^{4+} state is being maintained throughout the material bulk, if the compound is single-phase. It is also proven when looking at the complementary results of the more bulk-related techniques like the temperature-driven oxygen loss (O_2-TPD) and TEC measurements revealing the changes in the Fe oxidation state.

In the case of the Sr3d spectra (Figure S.4), three Sr states were distinguished and associated with the Sr contained within STF-x structure, SrO and $SrCO_3$ (with a characteristic peak at 289.5 eV in C1s spectra) [80–82]. Increasing the Sr content at A sublattice lead to decrease in the relative share of Sr forming the STF-x and increased its participation in the surficial formation of the SrO and, after reacting with atmospheric CO_2, the corresponding carbonate - $SrCO_3$. A superficial effect of the formation of $SrCO_3$ by the exposure for CO_2 was reported earlier and is closely related to the existence of surface SrO terminations in strontium titanates [40,66]. The presence of the $SrCO_3$ was confirmed by the XRD measurement. Based on the XPS, the total surface composition was determined. The introduction of Sr-deficiency leads to lowering of the surface Sr segregation. For Sr-deficient materials, the estimated surficial Sr content vs. (Ti + Fe) content was ~1, what stands for the formation for the non-segregated material or high homogeneity (Figure S.5). At the same time for stoichiometric material, this value reached ~1.3 indicating slight segregation of the Sr towards the surface. For highly Sr enriched materials, the surface Sr ratio peaked at the value of ~2 and thus indicated formation of the highly Sr surface-rich compound. Thus, one can correlate the Sr-stoichiometry in the lattice with the existence of the additional surface segregates of the Sr-base compounds.

After the deconvolution of the Ti2p spectra it was observed that titanium ions generally take up the Ti^{4+} valence (Fig. S.4). Each $2p_{3/2}$ peak of Ti2p spectra was situated at ~457.8 eV with the separation energy of 5.8 eV for the doublet. It clearly correspond to the Fe-doped $SrTiO_3$ lattice, what is in agreement with the previously obtained data by the research of Zhang S. L. et al. [43]. According to the studies on $SrTi_{0.7}Fe_{0.3}O_3$ performed by Nanning A. et al. [83] using Near Ambient Pressure XPS (NAP-XPS) the location of the $Ti2p_{3/2}$ peak depends on the surrounding atmosphere conditions. Under highly reducing conditions the peak is being shifted towards higher bonding energies of ~458.4 eV and while in oxidizing gases it is localized ~457.4 eV. Additionally, the $Ti2p_{1/2}$ peak is broadened, what is a typical behaviour of this feature.

Electrical properties

Total electrical conductivity was investigated as a function of temperature (from 900 °C to 200 °C) in different oxygen concentrations (1%, 5% and 20%). The results of the electrical measurements of the STF-x pellets are presented in Fig. 4 A).

According to the equation derived from the reaction of oxygen incorporation and mass action law [84] (Kröger–Vink notation), a concentration of electron holes can be expressed as:

$$p = \left(\frac{K}{[V''_{Sr}]}\right)^{\frac{1}{2}} x\, pO_2^{\frac{1}{4}} \qquad \text{(equation 1)}$$

where p denotes the concentration of electron holes, K denotes a chemical reaction constant, $[V''_{Sr}]$ is the concentration of strontium vacancies and pO_2 is an oxygen partial pressure. Based on Equation (1), it can be stated that the concentration of electron-holes and thus the conductivity of all STF-x

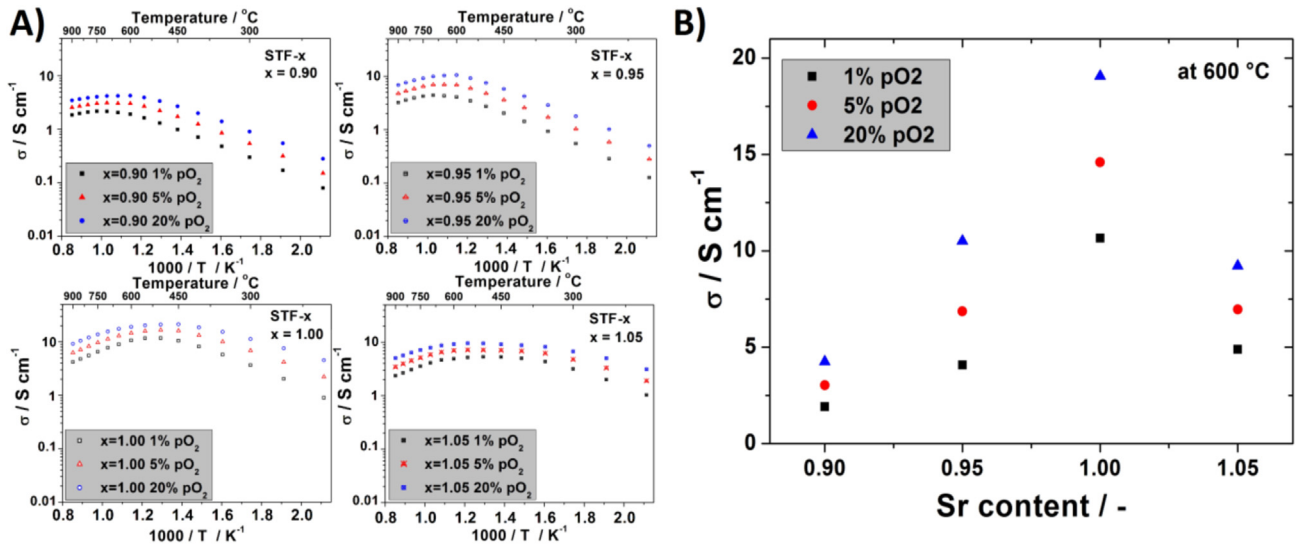

Fig. 4 – Electrical conductivity plots of sintered STF-x pellets measured at 20% O_2, 5% O_2 and 1% O_2 (A) and relation of conductivity at 600 °C as a function of Sr content (B).

decrease with the decreasing oxygen partial pressure. This is in agreement with the experimental results for all investigated samples (see Fig. 4 A). The results of STF-90, STF-95 and STF-100 also indicate a decrease of the conductivity with the increasing strontium deficiency (Fig. 4 B) similar as in the literature [57,58] and in qualitative agreement with equation (1). At 600 °C at 20% oxygen concentration, the conductivity of the STF-90 was ~4 S cm^{-1}, whereas for STF-100 its value was ~18 S cm^{-1}, thus the effect of the Sr-nonstoichiometry is considerable. This behaviour is also in line with equation (1), which relates the concentration of electron-holes inversely to the concentration of strontium vacancies.

The results for STF-105 can be influenced by the sample porosity and presence of secondary phases. As presented in Figure S.6 in the Supplementary materials, the density of STF-90/95/100 was >94%, whereas for the STF-105 the density was ~90%.

The temperature for the maximum conductivity increases slightly for the materials with the higher strontium deficiency (for STF-90 and STF-95 it is ~600 °C, and for STF-100 and STF-105 it is ~500 °C). Ni et al. also reported a slight change of the maximum conductivity temperature, but for their non-stoichiometric $Sr_{1-x}Ti_{0.3}Fe_{0.6}Ni_{0.1}O_{3-\delta}$, the maximum shift was 50 °C [55]. The shift might be correlated with the TG results and O_2-TPD, where the samples with higher Sr-deficiency showed decreased oxygen loss and delayed lattice oxygen evolution and thus decreased formation of charge balancing p-type carriers.

The chemical oxygen surface exchange (k*) and chemical diffusion (D*) coefficients were measured by the electrical conductivity relaxation (ECR) method. Due to the high sample density requirement, D* and k* were determined for STF-90, STF-95 and STF-100. Due to the porosity of the pellets after sintering, the STF-105 sample was not measured by ECR. The typical normalised data as a function of time for STF-90 and STF-100 measured at 700 °C is presented in Fig. 5 A). The total relaxation time at 700 °C was about 3000 s. Qualitatively, for all samples a faster equilibration time occurred during oxygen adsorption and incorporation (change from 10% pO_2 to 20% pO_2) than during desorption of oxygen (change from 20% pO_2 to 10% pO_2), which might indicate good performance of this material when used as an oxygen electrode in fuel cells.

The calculated values of chemical surface exchange coefficient k* and chemical oxygen diffusion coefficient D* are presented in Fig. 5 B)–C). At 700 °C, the values of k* are ~10^{-4} cm s^{-1} and D* from 10^{-5} to 10^{-6} cm^2 s^{-1}. The data is consistent with the values (from an ECR experiment) for STF50 reported by Schulze-Küppers [74]. Moreover, the chemical oxygen surface exchange coefficient of STF-x (at 800 °C) has a higher value than for the state-of-the-art $La_{0.6}Sr_{0.4}Co_{0.2}Fe_{0.8}O_{3-\delta}$ (~1.2×10^{-4}cm s^{-1}) [63].

In this work, k* at 800 °C for all STF-x (<9×10^{-3}cm s^{-1}) are one order of magnitude higher than the values obtained by Zhang et al. for $SrTi_{0.3}Fe_{0.7}O_{3-\delta}$ (~9×10^{-4} cm s^{-1}) [40], who, whoever, based their values on fitting of the electrochemical performance of the electrode to the Adler-Lane-Steele (ALS) model using detailed microstructural 3D analysis. This difference may be influenced by both other research methods for determining the value of k [44,85], as well as differences in the microstructure of the compounds [86] studied by Zhang et al. and in this work.

It was found that with an increasing strontium content, k* decreases (Fig. 5 D), whereas D* has the opposite trend. The calculated D* (~1×10^{-5}cm s^{-1}) for STF-x at 800 °C is similar to those reported for the $La_{0.6}Sr_{0.4}Co_{0.2}Fe_{0.8}O_{3-\delta}$ and $SrTiO_3$ materials [63,87]. In Fig. 5D) shows the relation between the chemical oxygen diffusion coefficient and the Sr content (at 700 °C). According to equation (1), increasing the Sr content increases the concentration of electron-holes, which may increase the chemical oxygen diffusion coefficient D*.

Electrochemical performance of $Sr_xTi_{0.3}Fe_{0.7}O_{3-\delta}$ oxygen electrodes

The results of EIS measurements and DRT analysis for symmetrical STF-x porous electrodes sintered at 800 °C, 900 °C and

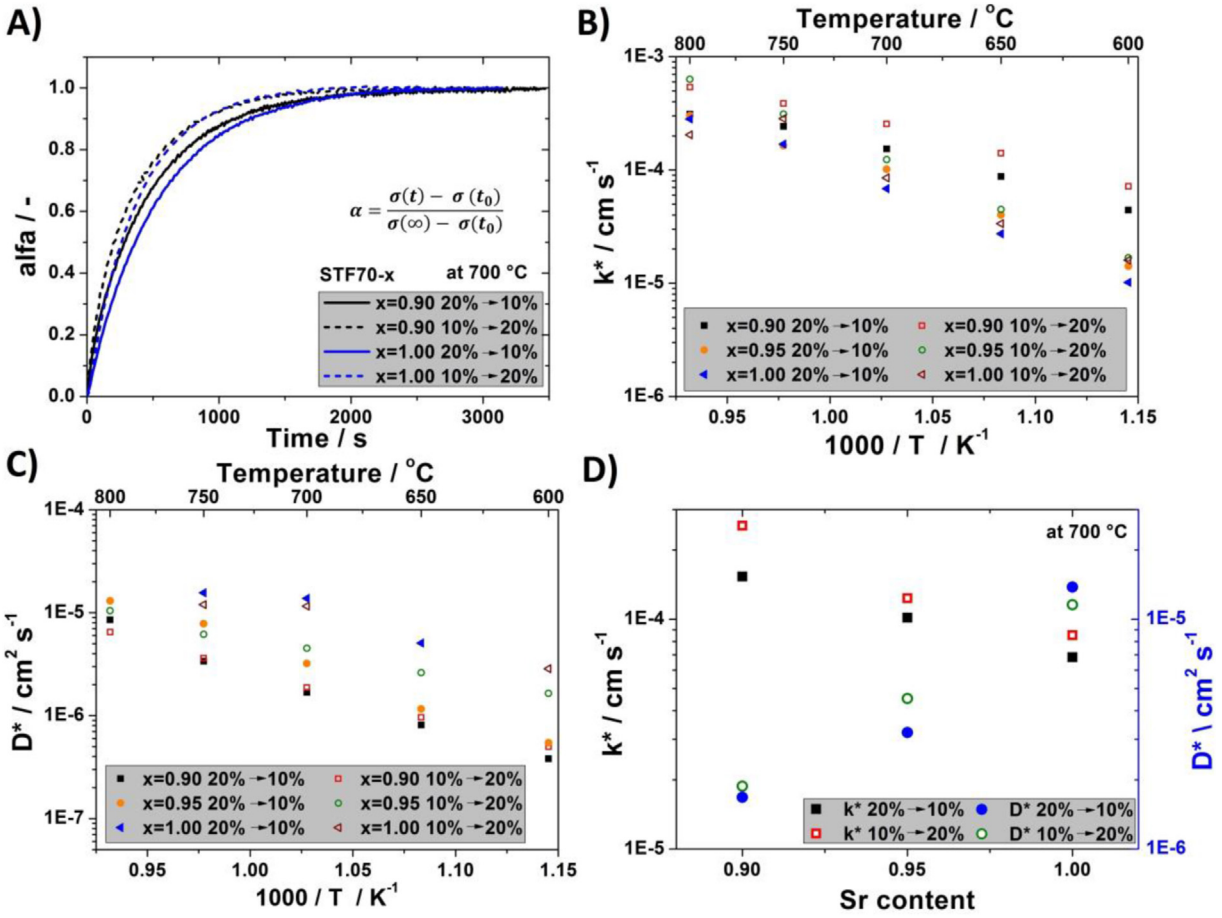

Fig. 5 – Exemplary normalised electrical conductivity relaxation plot of STF-x at 700 °C (A), calculated chemical oxygen surface exchange coefficient (B) and chemical oxygen diffusion coefficient (C) and relation between k* and D* as a function of Sr content at 700 °C.

1000 °C are presented in Fig. 6 A) and D); B) and E); C) and F), respectively.

The STF-x materials showed overall high electrochemical activity for oxygen reduction/evolution reactions. For electrodes sintered at 800 °C, the Area Specific Resistance (ASR) values measured at 700 °C in air were all within the range of ~55–94 mΩ cm^2, and were lower than that reported for $SrTi_{0.3}Fe_{0.7}O_{3-\delta}$ (112 mΩ cm^2) [40] or $Sr_{1-x}Ti_{0.3}Fe_{0.6}Ni_{0.1}O_{3-\delta}$ (~220 mΩ cm^2) [55] obtained in similar conditions. The electrode performance below 150 mΩ cm^2 is promising for high performance SOCs [88]. For the Co-containing $Sr(Ti_{0.3}Fe_{0.7-x}Co_x)O_{3-\delta}$ reported by Zhang et al. ASR values of 40–90 mΩ cm^2 were achieved [43]. For higher sintering temperatures, the Sr-deficient STF-90 and STF-95 show slightly worse performance than the STF-100 and STF-105. Interestingly, the highest performance among the tested electrodes was achieved for the STF-105 sintered at 900 °C. Even though the powder contained traces of strontium carbonate (detected by XRD) and the surface was enriched in strontium (detected by XPS), its ORR/OER performance was the highest, i.e. the polarisation resistance was the lowest (~55 mΩ cm^2 at 700 °C). The specific reasons are not so obvious and are open to future research.

For the sintering temperature of 800 °C, the area specific resistance (ASR) values were comparable for all STF-x electrodes, but as the sintering temperature increased, the differences in electrode performance also increased. The STF-90 was the most sensitive electrode to the effect of the sintering temperature, in contrast to the STF-105 (Figure S.7). For the sintering temperature of 1000 °C, the Sr-deficient compounds (STF-90 and STF-95) have almost twice the value of ASR in comparison to the STF-100 or STF-105. The change in electrochemical performance might come from the formation of a dense, interfacial layer, observed by SEM for STF-90 and STF-95 (Figure S.8). The high Sr content and its surface segregation hinders sintering of the electrodes and has a positive effect on the electrode performance.

The sintering temperature conditions for the preparation of the STF-90, STF-95 and STF-100 electrodes had no significant impact on the ohmic resistance (Figure S.9) as we reported earlier for $SrTi_{0.3}Fe_{0.7}O_{3-\delta}$ [62]. The STF-105 slightly improved contact with the electrolyte with the increasing sintering temperature. Even though the electrical conductivity of the STFx materials is quite low (1–20 S cm^{-1} at 700 °C), this seems sufficient to provide good current collection in the measurements.

These results show, that the electrochemical performance of STFx materials can be tuned by A-site non-stoichiometry and sintering conditions. The obtained ASR values are

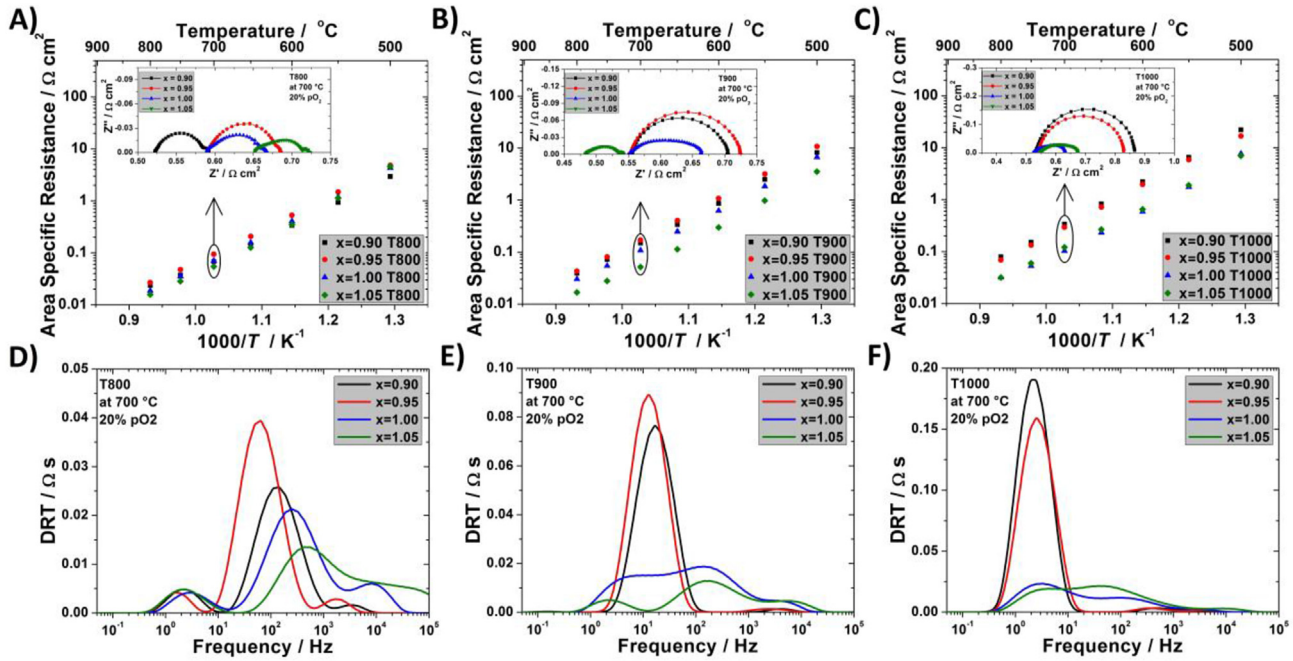

Fig. 6 – Impact of Sr non-stoichiometry on polarisation resistances of symmetrical cells with STF-x electrodes sintered at 800 °C, 900 °C and 1000 °C, respectively (A–C) and corresponding distribution of relaxation times results (D–F) for EIS spectra measured in 20% O_2 at 700 °C.

comparable to typical polarisation values reported for MIEC oxygen electrodes in the intermediate-temperature range [89,90], e.g. 0.1–1 Ωcm2 at 600–700 °C.

Distribution of relaxation times analysis

The results of the DRT analysis (Fig. 6 D)–F)) corresponding to the EIS spectra obtained at 700 °C in air (insets of Fig. 6 A)–C)) indicate differences in electrochemical processes depending on the Sr content.

For all STF-x sintered at the lowest temperature (800C °C), there are possibly two peaks related to two electrochemical processes, as also reported in our previous work for $SrTi_{0.3}Fe_{0.7}O_{3-\delta}$ [61]. The low frequency peak (~1 Hz) is similar for all electrode materials and is most probably connected to gas diffusion within the porous electrodes. The main electrochemical process has a characteristic peak at the frequency of 30–300 Hz (middle frequency), depending on the compound. The lowest contribution and the highest characteristic frequency were obtained for STF-105. The contributions visible as higher frequency "shoulders" of lower magnitude might be indicative of Gerischer-type elements, typically considered for MIEC perovskite electrodes in this frequency range.

As the sintering temperature increased, the spectra changed shape. For the STF-90 and STF-95, only a single process became distinguishable in the DRT spectra (Fig. 6 E) and F)). The shape of the DRT spectrum for STF-100 and STF-105 seems to be insensitive to the sintering temperature and shows the gas diffusion and higher frequency contributions.

To evaluate the electrochemical processes for the STF-90 and STF-95 in more detail, the responses of the electrodes sintered at 900 °C were also investigated at 700 °C as a function of oxygen partial pressure (pO_2). Fig. 7 A)–B) presents the selected EIS spectra and corresponding DRT spectra for the STF-90 at different oxygen concentrations. Similar results were achieved for the STF-95. The EIS measurement data were fitted by an equivalent circuit that consists of two R-CPE elements due to the occurrence of a low frequency contribution visible only at low pO_2 values (<5% O_2).

The ohmic resistance (R_s), low frequency resistance (R_{gas}), middle frequency resistance (R_1) and R-CPE calculated equivalent pseudo capacitances for the STF-90 and STF-95 as a function of oxygen partial pressure are presented in Fig. 7C)–F) and listed in Table S.2 and Table S.3. For pseudo capacitance calculation this formula was used:

$$C = \frac{(R*Y)^{\frac{1}{n}}}{R} \qquad \text{(equation 2)}$$

where C is pseudo capacitance, R resistance of R-CPE element, Y capacitance of R-CPE element and n is dimensionless value. Additionally, for comparison, the results of the pseudo capacitance for the stoichiometric STF-100 at 20% pO_2, reported earlier [61], are presented in Fig. 7F) and measured in this work for the STF-100 in the same conditions.

The fitting results reveal similarities for both Sr-deficient compounds. On the other hand, there are visible differences in comparison to the stoichiometric $SrTi_{0.3}Fe_{0.7}O_{3-\delta}$. Changes of the ohmic resistance in the function of pO_2 are negligible, because the CGO substrates are being practically insensitive for oxygen partial changes under the conditions used within this study [61]. The values for both STF-x compounds are comparable, taking into account the precision of 10% variation in the thickness of the electrolyte. As in our previous work, R_{gas} strongly depends on the oxygen concentration and the slope of the double logarithmic plot (n = −1), suggesting that it is indeed a gas diffusion process. In the case of R_1 and C_1, the value of pseudo capacitance

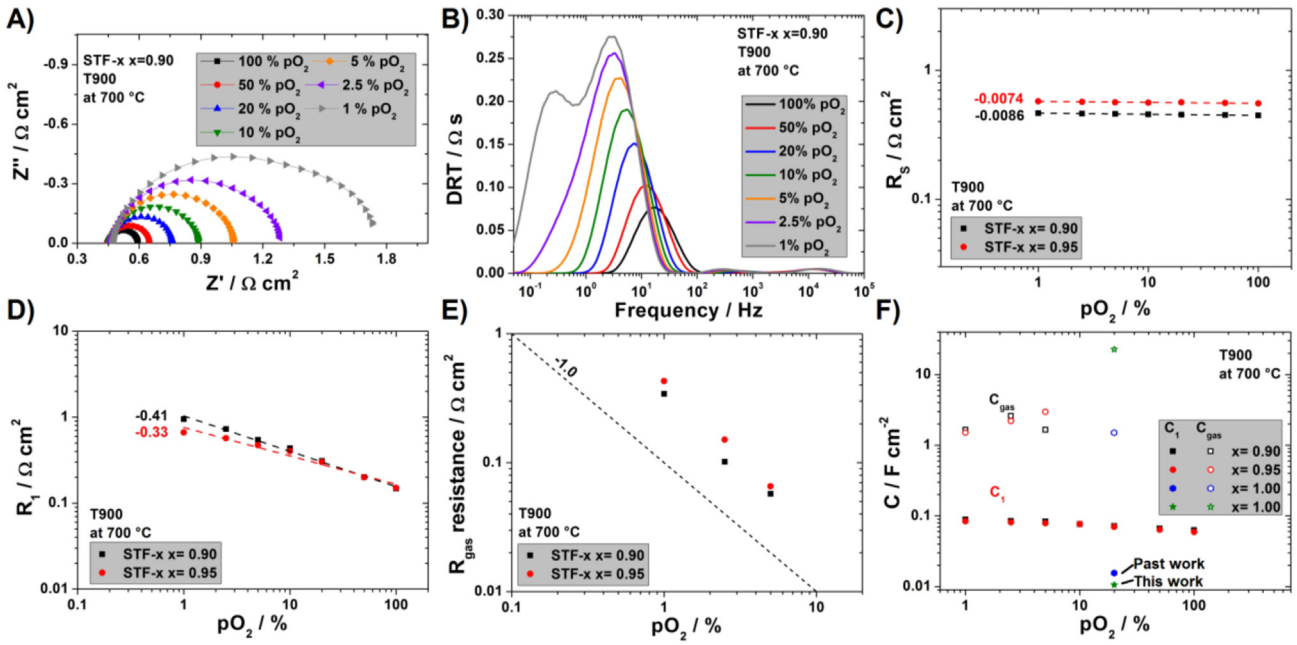

Fig. 7 – Results of EIS measured at 700 °C and different oxygen partial pressures for STF-90 symmetrical cells (A) and corresponding DRT spectra (B), values of calculated contribution of series resistance (C), R1 (D) and R_{gas} (E) and relayed pseudo capacitances (F) as a function of oxygen partial pressure for STF70-90 and STF70-95.

revealed a one order of magnitude increase in relation to the STF-100. The Sr-deficient materials show pseudo capacitance in the range of ~0.1 F cm^{-2}, whereas the stoichiometric STF70 showed a pseudo capacitance of ~0.01 F cm^{-2}, which is probably connected to the formation of a dense interfacial layer at temperatures of 900 °C and above for the Sr-deficient electrode materials and its chemical capacitance due to the accumulation of electro-active oxygen species (oxygen vacancies) in the "bulk" of the thin film structure [91]. This dense layer modifies the ORR/OER process at the interface between the ionic conductor (CGO) and MIEC electrode (STF70).

Solid oxide fuel cell test

The influence of strontium non-stoichiometry on the performance of solid oxide fuel cells at 700 °C was also checked. For the tests, Sr-deficient STF-95 sintered at 800 °C and Sr-enriched STF-105 sintered at 1000 °C were selected. The higher sintering temperature of STF-105 was chosen due to the lower sinterability of this compound. The reference cell with an LSCF cathode was sintered at 1050 °C. Fig. 8 A)–B) shows the current-voltage characteristics (I–V) and EIS for the tested fuel cells. For comparison, the I–V and EIS characteristics for the STF-100 are presented at Figure S.10. The maximum power density for fuels with STF-95, STF-105 and LSCF cathodes were, respectively: 809 mW cm^{-2}, 594 mW cm^{-2}, and 1206 mW cm^{-2}. Although the EIS measurements revealed that all of the materials have different value of polarisation resistance (STF-95 – 276 mΩ cm^2, STF-105 – 337 mΩ cm^2, and LSCF – 237 mΩ cm^2), the electrochemical processes at 700 °C (syn. air and wet H_2) are probably the same, as studied by DRT (presented in Figure S.11 A)). Differences are observed also for the ohmic resistances. The lowest R_s was measured for the LSCF (115 mΩ cm^2), followed by the STF-95 (247 mΩ cm^2), and the STF-105 (261 mΩ cm^2). The increased ohmic resistance originates from the STF materials, which have much lower electronic conductivity than LSCF. Thus, the inferior performance of the cells with STF in comparison to the cells with LSCF is determined by the ohmic resistance. Interestingly, considering only STF-x materials the difference for ASR of symmetrical samples between STF-95 (sintered at 800 °C) and STF-105 (sintered at 1000 °C) was ~29.8% (94 mΩ cm^2 and 122 mΩ cm^2 respectively). In SOFC applications difference of polarisation resistances decrease up to ~22.1%. In the case of ohmic resistance, symmetric samples showed identical value 1.1 Ω cm^2 but in SOFC it slightly change (~5.7%) in favor of STF-95. Which explains the better performance of cells with STF-95 material than with STF-105.

For a more detailed investigation of the influence of Sr non-stoichiometry on electrochemical processes of STF-x materials in fuel cells, EIS measurements as a function of pO_2 were carried out. The results of the DRT analysis corresponding to the EIS data at different pO_2 (Figure S.11 B)–C)) are presented in Fig. 8 C). Three main peaks can be observed. The low-frequency peak (~1 Hz) is probably related to gas diffusion on the cathode and anode side. This low frequency peak looks similar for both cells at 20% and 50% of oxygen partial pressure, but the fuel cell with the STF-105 cathode seems be more sensitive to lowering the pO_2. In contrast, the middle frequency peak (~100 Hz) at low pO_2 (3% pO_2) is comparable for both cells and with the increasing oxygen partial pressure, the fuel cell with the STF-95 cathode decreased more (practically disappearing at 50% of pO_2). This frequency is often attributed to oxygen incorporation and diffusion (e.g. typical Gerischer element). This result is in line with the higher k* value for strontium-deficient materials. For the high frequency peak

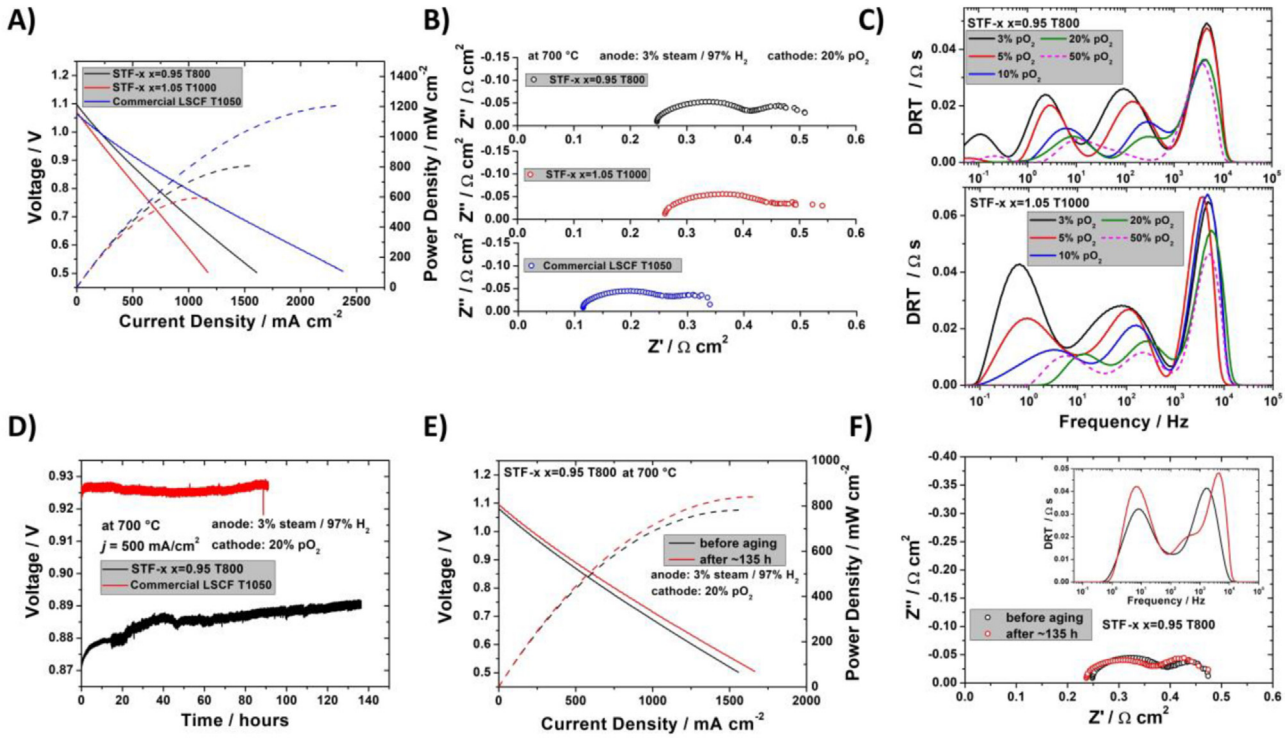

Fig. 8 – I–V characteristic of anode-supported cells (A), Nyquist plots of impedance data measured at OCV (B), DRT analysis of EIS measured as a function of pO_2 for cells with the STF-x cathodes (C), cell stability test under 0.5 A cm^{-2} current load (D) I–V plot before and after ageing of the fuel cell with the STF-95 cathode (E) and corresponding EIS (F).

(~5000 Hz), an observable small decrease of the peak for 20% and 50% of pO_2 in contrast to the rest of the tested conditions can be noticed. Even though the high frequency peak is larger for the cell with the STF-105 cathode, the trend for both cells is comparable, and this peak is probably connected with ion transfer across the cathode/electrolyte.

The performance of the STF-95 and the reference LSCF cathode was evaluated by monitoring the cell voltage output under a constant current load of 0.5 A cm^{-2} (Fig. 8 D) as a function of time. The initial voltages were ~0.87 V and ~0.93 V for the cell with the STF-95 and LSCF cathodes, respectively. During the 136-h the test, the voltage of the cell with the STF-95 cathode steadily increased by 0.02 V and it seems that it did not reach its maximum. In the case of the cell with the LSCF cathode, the voltage was almost stable over the 90 h of the test. The I–V and EIS measurements before and after the ageing test of the cell with the STF-95 cathode revealed improvement of the maximum power density and ohmic resistance with a concurrent small increase of ASR (Fig. 8 E)–F)). Based on the SEM images taken before and after the stability test (Fig. S. 12), there are visible small difference of microstructure between two materials. STF-95 sintered at 800 °C present smaller grains than LSCF sintered at 1050 °C what was to be expected. Interestingly, both materials did not show significant changes in grain size, and no layer formed at the interface. Although the electrical results indicate the advantage of LSCF, STF-95 has the potential to be further modified, for example by infiltration, which will most likely allow it to be taken into account as a potential electrode for SOFCs.

Discussion

Modifications at the A-site sublattice of STF-x material lead to important modifications of the main material properties (e.g. TEC, k*, D*, and σ) which in turn leads to differences in ASR values (Fig. 9A)).

One interesting feature of such modification is that electrochemical performance of the porous Sr-deficient materials can be easily limited by a too-high sintering temperature and the formation of a dense interface layer (Fig. 9 A) blue frame). The thickness of the dense interface layers formed at the sintering temperature of 900 °C for the STF-90 electrode was ~200 nm, whereas for the STF-95 it was slightly thinner (~150 nm). The formation of this dense layer has also been confirmed by Yang et al. [59]. In that case, the layer formed at higher temperatures, probably due to the use of larger particles.

The dense interfacial layer clearly shows a chemical capacitance that depends on the oxygen storage capacity. For example, the chemical capacitance of STF5, STF35 and STF50 thin films was studied by Jung and Tuller [92]. They found a strong dependence of the capacitance on the iron content. For the same thickness of thin films, the capacitance of STF50 was almost an order of magnitude higher than for STF35, for which a value of ~12 mF cm^{-2} for a 160 nm thick layer was reported at 650 °C. Considering the higher content of oxygen vacancies for a higher Fe composition (STF70 instead of STF50) and extra vacancies due to Sr-nonstoichiometry (for lower temperatures), the capacitance of the layer is in reasonable agreement

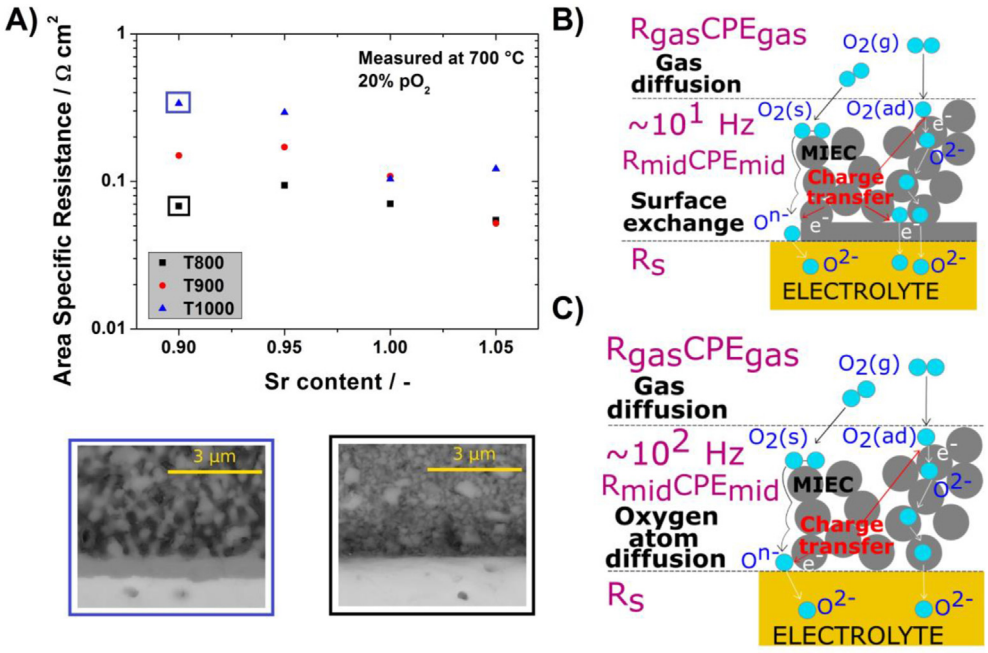

Fig. 9 – ASR as a function of strontium content for different sintering temperatures and SEM pictures of selected materials indicating significant microstructure differences (A), proposed model for porous STF-x cathode (B) and STF-x with a dense layer (C).

with the literature-proposed model for a thin film electrode with surface exchange-limited performance [91,92].

For materials sintered at low temperature (800 °C), characterised by a porous microstructure, the limiting electrochemical step is the process occurring at the middle frequency, identified as the adsorbed oxygen atom surface diffusion followed by a charge transfer reaction and incorporation into the lattice (Fig. 9C)) [61,93]. As presented in Fig. 6 D), the contribution of the middle frequency peaks for the STF-90 and STF-95 is larger than for the STF-100 and STF-105, which is in line with the presented changes of D*. In the case of the STF-90 and STF-95 sintered at higher temperatures (≥900 °C), where Sr-non-stoichiometry induced the formation of a thin interface layer, the limiting electrochemical process changed to a surface exchange/bulk diffusion-limited process due to the lower apparent surface area of the dense layer (Fig. 9 B)). Interestingly, the highest electrochemical performance, measured in the symmetrical cell test, was obtained for the STF-105 electrode, which has a high surface content of Sr confirmed by XPS. It seems that the extra porosity, caused by inferior sinterability, led to the lowest ASR.

The maximum power density of the tested solid oxide fuel cell with STF-95 and STF-105 cathodes with similar microstructures (without a dense layer) differ (809 mW cm^{-2}, 594 mW cm^{-2}), which is in agreement with the results obtained for EIS (94 mΩ cm^2, 122 mΩ cm^2) for the symmetrical cells. The cell with the STF-95 cathode, with higher k*, showed increased performance in the intermediate frequency range (Fig. 8C). The results of the cell performance with the new Co-free oxygen electrode are encouraging. To even further improve the functional properties, it is of interest to increase the total electronic conductivity of the electrode, e.g. by mixing with different material or by infiltration by highly conductive phases.

Summary

In this work, the complex nature of the influence of the Sr-non-stoichiometry on the structural, transport and electrocatalytic properties of the promising $Sr_xTi_{0.7}Fe_{0.3}O_{3-\delta}$-based materials was investigated.

The results showed that modification of the chemical composition by the introduction of non-stoichiometry affects the lattice parameter, i.e. a decrease of the Sr content results in a unit cell parameter increase, which has been connected (via XPS) to the reduction of Fe^{4+} to Fe^{3+} by the charge compensation mechanism and the introduction of oxygen vacancies. Lowering of the concentration of A-site cations (bulk Sr content) lowers the Sr-surface segregation. Based on XPS results, the Sr content is inversely correlated with the Fe^{+3}/Fe^{+4} ratio. Sr-deficient powders contained a lower amount of Fe^{4+} available for thermal reduction at higher temperatures. This was further confirmed by the thermogravimetry (TG), dilatometry (DIL) and temperature programmed (TPx) methods, which revealed changes in weight loss on heating and a lower thermal expansion coefficient due to the lower amount of strontium. One of the issues reported with STF materials with high iron content is their relatively high thermal expansion coefficient. Tailoring the Sr-stoichiometry can limit the TEC from ~21 to ~17, which is a marked improvement for practical applications at intermediate temperature. In accordance with the existing defect model of STF, the introduction of Sr-deficiency results in decreased electronic (p-type) conductivity [65].

The electrocatalytic performance of bulk materials, as determined by the ECR technique, showed a positive influence of the Sr-deficiency on chemical surface exchange

coefficient (k*), and a negative effect on the chemical diffusion coefficient of oxygen (D*). In the electrochemical evaluation of porous electrodes, a complex trend in materials behaviour was found. Electrodes sintered at 800 °C showed similar electrochemical processes, with at least two clearly separated processes. Due to the small particle size of the synthesised powders and increased sinterability of the Sr-deficient materials, a continuous interfacial layer is formed even at sintering temperatures of 900 °C and above. This layer negatively influenced the electrode performance. Interestingly, the best overall electrode performance (~50 mΩ cm^2 at 700 °C, including the contribution of gas diffusion) was obtained for Sr-rich material (STF-105). Even though the electrical conductivity of this compound was inferior to the stoichiometric one and it showed high surface Sr segregation, its performance was clearly superior. This high performance was attributed to the decreased sinterability of these materials, which restricted grain growth and maintained a high surface area available for oxygen reduction and oxidation processes.

Based on these results, rational design of electrode materials through tailoring A-site non-stoichiometry of the perovskites, based on $Sr_xTi_{0.3}Fe_{0.7}O_{3-\delta}$ (x = 0.90; 0.95; 1.00; 1.05) is possible, but the relation between the basic physicochemical properties of bulk materials and porous electrode materials is complex. Even the well-studied issue of Sr-surface segregation requires further investigation to fully elucidate its effects. Moreover, the solid oxide fuel cell test confirmed that Sr-deficient STF-x materials could be a viable alternative for Co-containing state-of-the-art materials after improvement of the ohmic resistance by, e.g., impregnation.

Availability of data and material

The data that support the findings of this study are openly available in The MOST Wiedzy Open Research Data Catalog at 10.34808/yhx3-f485, reference number [94].

Authors' contributions

A.M.: Investigation; Data curation; Visualization; Writing - original draft.

S.M.: Conceptualization; Methodology; Writing - review & editing.

P.B.: Investigation; Data curation; Writing - original draft;

T.M.: Conceptualization; Methodology; Validation;

K.G.: Investigation; Data curation;

J.K.: Investigation; Data curation;

P.J.: Methodology; Resources; Writing - review & editing; Supervision; Funding acquisition.

Declaration of competing interest

The authors declare that they have no known competing financial interests or personal relationships that could have appeared to influence the work reported in this paper.

Acknowledgements and Funding

This work was supported by a project funded by National Science Centre Poland based on decision 2017/25/B/ST8/02275. Funding from Statutory Research funds at WETI PG is also acknowledged.

Appendix A. Supplementary data

Supplementary data to this article can be found online at https://doi.org/10.1016/j.ijhydene.2023.05.323.

REFERENCES

[1] Ahmad MZ, Ahmad SH, Chen RS, Ismail AF, Hazan R, Baharuddin NA. Review on recent advancement in cathode material for lower and intermediate temperature solid oxide fuel cells application. Int J Hydrogen Energy 2022;47:1103–20. https://doi.org/10.1016/j.ijhydene.2021.10.094.

[2] Zhang Y, Nicholas JD. Updating the notion that poor cathode performance typically dominates overall solid oxide fuel cell response. J Electrochem Soc 2021;168:034513. https://doi.org/10.1149/1945-7111/abed21.

[3] Yan D, Liang L, Yang J, Zhang T, Pu J, Chi B, Li J. Performance degradation and analysis of 10-cell anode-supported SOFC stack with external manifold structure. Energy 2017;125:663–70. https://doi.org/10.1016/j.energy.2016.12.107.

[4] Lee YH, Chang I, Cho GY, Park J, Yu W, Tanveer WH, Cha SW. Thin film solid oxide fuel cells operating below 600°C: a review. Int. J. Precis. Eng. Manuf. - Green Technol. 2018;5:441–53. https://doi.org/10.1007/s40684-018-0047-0.

[5] Hagen A, Liu YL, Barfod R, Hendriksen PV. Assessment of the cathode contribution to the degradation of anode-supported solid oxide fuel cells. J Electrochem Soc 2008;155:B1047. https://doi.org/10.1149/1.2960938.

[6] Zurlo F, Natali Sora I, Felice V, Luisetto I, D'Ottavi C, Licoccia S, Di Bartolomeo E. Copper-doped lanthanum ferrites for symmetric SOFCs. Acta Mater 2016;112:77–83. https://doi.org/10.1016/j.actamat.2016.04.015.

[7] Zhou W, Ran R, Shao Z. Progress in understanding and development of Ba0.5Sr0.5Co0.8Fe0.2O3-δ-based cathodes for intermediate-temperature solid-oxide fuel cells: a review. J Power Sources 2009;192:231–46. https://doi.org/10.1016/j.jpowsour.2009.02.069.

[8] Bai J, Han Z, Zhou D, Zhu X, Wang N, Chen R, He J, Yan W. Preparation of Pr2NiO4+δ-La0.6Sr0.4CoO3-δ as a high-performance cathode material for SOFC by an impregnation method. Int J Hydrogen Energy 2023;48:6076–87. https://doi.org/10.1016/j.ijhydene.2022.11.123.

[9] Zhang Y, Knibbe R, Sunarso J, Zhong Y, Zhou W, Shao Z, Zhu Z. Recent progress on advanced materials for solid-oxide fuel cells operating below 500 °C. Adv Mater 2017;29. https://doi.org/10.1002/adma.201700132.

[10] Irshad M, Idrees R, Siraj K, Shakir I, Rafique M, ul Ain Q, Raza R. Electrochemical evaluation of mixed ionic electronic perovskite cathode LaNi1-xCoxO3-δ for IT-SOFC synthesized by high temperature decomposition. Int J Hydrogen Energy 2021;46:10448–56. https://doi.org/10.1016/j.ijhydene.2020.09.180.

[11] Lee J, Choi M, Lee W. Encapsulation of metal catalysts for stable solid oxide fuel cell cathodes. Int. J. Precis. Eng. Manuf.

- Green Technol. 2021;8:1529–35. https://doi.org/10.1007/s40684-020-00290-8.
[12] Yang Q, Tian D, Liu R, Wu H, Chen Y, Ding Y, Lu X, Lin B. Exploiting rare-earth-abundant layered perovskite cathodes of LnBa0.5Sr0.5Co1.5Fe0.5O5+δ (Ln=La and Nd) for SOFCs. Int J Hydrogen Energy 2021;46:5630–41. https://doi.org/10.1016/j.ijhydene.2020.11.031.
[13] Cai W, Cao D, Zhou M, Yan X, Li Y, Wu Z, Lü S, Mao C, Xie Y, Zhao C, Yu J, Ni M, Liu J, Wang H. Sulfur-tolerant Fe-doped La0·3Sr0·7TiO3 perovskite as anode of direct carbon solid oxide fuel cells. Energy 2020;211:118958. https://doi.org/10.1016/j.energy.2020.118958.
[14] Choi M, Lee J, Lee W. Fluid mechanical approaches for rational design of infiltrated electrodes of solid oxide fuel cells. Int. J. Precis. Eng. Manuf. - Green Technol. 2019;6:53–61. https://doi.org/10.1007/s40684-019-00021-8.
[15] Kharton VV, Figueiredo FM, Kovalevsky AV, Viskup AP, Naumovich EN, Jurado JR, Frade JR. Oxygen diffusion in, and thermal expansionof, $SrTiO_{3-\delta}$- and $CaTiO_{3-\delta}$-Based materials. Defect Diffusion Forum 2000;186–187:119–36. https://doi.org/10.4028/www.scientific.net/ddf.186-187.119.
[16] Niemczyk A, Olszewska A, Du Z, Zhang Z, Świerczek K, Zhao H. Assessment of layered La2-x(Sr,Ba)xCuO4-δoxides as potential cathode materials for SOFCs. Int J Hydrogen Energy 2018;3. https://doi.org/10.1016/j.ijhydene.2018.06.119.
[17] Ni W, Zhu T, Chen X, Jin C, Bu Y, Zhong Q, Han M. Coupling decreased polarization resistance Sr0.95Ti0.3Fe0.6Ni0.1O3-δ cathode with efficient metal supported Solid Oxide Fuel Cell. J Power Sources 2021;489:229490. https://doi.org/10.1016/j.jpowsour.2021.229490.
[18] Li Q, Cao G, Zhang X, Li G. Topology optimization of the microstructure of solid oxide fuel cell cathodes. Acta Mater 2020;201:278–85. https://doi.org/10.1016/j.actamat.2020.10.003.
[19] Morall E. Manganese oxides/LaMnO 3 perovskite materials and their application in the oxygen reduction reaction. Energy 2022;247. https://doi.org/10.1016/j.energy.2022.123456.
[20] Barros Julião PS. A-site cation influences on performance, structure and conductivity of a lanthanide-based perovskite electrode for symmetrical solid oxide fuel cells. J Power Sources 2020;450. https://doi.org/10.1016/j.jpowsour.2020.227723.
[21] Gao J, Ma D, Zhao H, Li Q, Lü Z, Wei B. Synergistically improving electrocatalytic performance and CO2 tolerance of Fe-based cathode catalysts for solid oxide fuel cells. Energy 2022;252:124050. https://doi.org/10.1016/j.energy.2022.124050.
[22] Meng Y, Zhang W, He Z, Liu C, Gao J, Akbar M, Guo R, Zhou S, Ji Y, Wang X, Yang Y. Partially reduced Ni0.8Co0.15Al0.05LiO2-δ for low-temperature SOFC cathode. Int J Hydrogen Energy 2021;46:9874–81. https://doi.org/10.1016/j.ijhydene.2020.05.150.
[23] Khurana S, Johnson S, Karimaghaloo A, Lee MH. Effect of sintering process with Co3O4 on the performance of LSCF-based cathodes for solid oxide fuel cells. Int. J. Precis. Eng. Manuf. - Green Technol. 2018;5:637–42. https://doi.org/10.1007/s40684-018-0066-x.
[24] Lyu Z, Li H, Han M. Electrochemical properties and thermal neutral state of solid oxide fuel cells with direct internal reforming of methane. Int J Hydrogen Energy 2019;44:12151–62. https://doi.org/10.1016/j.ijhydene.2019.03.048.
[25] Chen G, Wang Y, Sunarso J, Liang F, Wang H. A new scandium and niobium co-doped cobalt-free perovskite cathode for intermediate-temperature solid oxide fuel cells. Energy 2016;95:137–43. https://doi.org/10.1016/j.energy.2015.11.061.
[26] Clematis D, Barbucci A, Presto S, Viviani M, Carpanese MP. Electrocatalytic activity of perovskite-based cathodes for solid oxide fuel cells. Int J Hydrogen Energy 2019;44:6212–22. https://doi.org/10.1016/j.ijhydene.2019.01.128.
[27] Yu W, Lee Y, Lee YH, Cho GY, Park T, Tanveer WH, Kim Y, Cha SW. Performance enhancement of thin film LSCF cathodes by gold current collecting layer. Int. J. Precis. Eng. Manuf. - Green Technol. 2016;3:185–8. https://doi.org/10.1007/s40684-016-0024-4.
[28] Baharuddin NA, Mohd Nazrul Aman NA, Muchtar A, Somalu MR, Abdul Samat A, Aznam MI. Structural, morphological, and electrochemical behavior of titanium-doped SrFe 1-x Ti x O 3-δ (x = 0.1–0.5)perovskite as a cobalt-free solid oxide fuel cell cathode. Ceram Int 2019;45:12903–9. https://doi.org/10.1016/j.ceramint.2019.03.216.
[29] Fan W, Sun Z, Bai Y, Wu K, Zhou J, Cheng Y. In situ growth of nanoparticles in A-site deficient ferrite perovskite as an advanced electrode for symmetrical solid oxide fuel cells. J Power Sources 2020;456:228000. https://doi.org/10.1016/j.jpowsour.2020.228000.
[30] Baharuddin NA, Muchtar A, Somalu MR, Kalib NS, Raduwan NF. Synthesis and characterization of cobalt-free SrFe0·8Ti0·2O3-δ cathode powders synthesized through combustion method for solid oxide fuel cells. Int J Hydrogen Energy 2019;44:30682–91. https://doi.org/10.1016/j.ijhydene.2018.11.142.
[31] Liu Y, Motalov V, Baumann S, Sergeev D, Müller M, Sohn YJ, Guillon O. Thermochemical stability of Fe- and co-functionalized perovskite-type SrTiO3 oxygen transport membrane materials in syngas conditions. J Eur Ceram Soc 2019;39:4874–81. https://doi.org/10.1016/j.jeurceramsoc.2019.06.045.
[32] Schulze-Küppers F, Baumann S, Meulenberg WA, Bouwmeester HJM. Influence of support layer resistance on oxygen fluxes through asymmetric membranes based on perovskite-type oxides SrTi1-xFexO3-δ. J Membr Sci 2020;596:117704. https://doi.org/10.1016/j.memsci.2019.117704.
[33] Yin XB, Tan ZH, Yang R, Guo X. Single crystalline SrTiO3 as memristive model system: from materials science to neurological and psychological functions. J Electroceram 2017;39:210–22. https://doi.org/10.1007/s10832-017-0083-0.
[34] Rothschild A, Litzelman SJ, Tuller HL, Menesklou W, Schneider T, Ivers-Tiffée E. Temperature-independent resistive oxygen sensors based on SrTi1-xFexO3-δsolid solutions. Sens Actuators, B 2005;108:223–30. https://doi.org/10.1016/j.snb.2004.09.044.
[35] Li HY, Yang H, Guo X. Oxygen sensors based on SrTi0.65Fe0.35O3-δthick film with MgO diffusion barrier for automotive emission control. Sens Actuators, B 2015;213:102–10. https://doi.org/10.1016/j.snb.2015.02.079.
[36] Dayaghi AM, Kim KJ, Kim SJ, Sung YS, Choi GM. Oxidation of porous stainless-steel coated with donor-doped SrTiO3 in anodic atmosphere of solid oxide fuel cell. J Power Sources 2017;360:488–94. https://doi.org/10.1016/j.jpowsour.2017.06.017.
[37] Tkach A, Okhay O, Almeida A, Vilarinho PM. Giant dielectric permittivity and high tunability in Y-doped SrTiO3 ceramics tailored by sintering atmosphere. Acta Mater 2017;130:249–60. https://doi.org/10.1016/j.actamat.2017.03.051.
[38] Anh LD, Kaneta S, Tokunaga M, Seki M, Tabata H, Tanaka M, Ohya S. High-mobility 2D hole gas at a SrTiO3 interface. Adv Mater 2020;32:1–7. https://doi.org/10.1002/adma.201906003.
[39] Kang KT, Kang H, Park J, Suh D, Choi WS. Quantum conductance probing of oxygen vacancies in SrTiO3 epitaxial thin film using graphene. Adv Mater 2017;29. https://doi.org/10.1002/adma.201700071.
[40] Zhang S-L, Cox D, Yang H, Park B-K, Li C-X, Li C-J, Barnett SA. High stability SrTi 1−x Fe x O 3−δ electrodes for oxygen reduction and oxygen evolution reactions. J Mater Chem A 2019;7:21447–58. https://doi.org/10.1039/C9TA07548H.

[41] Jia C, Ma Q, Han M, Wang W, Menzler NH, Guillon O. Fabrication and performance of La, Co-substituted SrTiO 3 as cathode materials of solid oxide fuel cell. ECS Trans 2019;91:1291–8. https://doi.org/10.1149/09101.1291ecst.
[42] Zhu T, Troiani H, Mogni LV, Santaya M, Han M, Barnett SA. Exsolution and electrochemistry in perovskite solid oxide fuel cell anodes: role of stoichiometry in Sr(Ti,Fe,Ni)O3. J Power Sources 2019;439:227077. https://doi.org/10.1016/j.jpowsour.2019.227077.
[43] Zhang SL, Wang H, Lu MY, Zhang AP, Mogni LV, Liu Q, Li CX, Li CJ, Barnett SA. Cobalt-substituted SrTi0.3Fe0.7O3-: δ a stable high-performance oxygen electrode material for intermediate-temperature solid oxide electrochemical cells. Energy Environ Sci 2018;11:1870–9. https://doi.org/10.1039/c8ee00449h.
[44] Skiba EJ, Chen T, Perry NH. Simultaneous electrical, electrochemical, and optical relaxation measurements of oxygen surface exchange coefficients: Sr(Ti,Fe)O3-d film crystallization case study. ACS Appl Mater Interfaces 2020;12:48614–30. https://doi.org/10.1021/acsami.0c14265.
[45] Lan C, Luo J, Dou M, Zhao S. First-principles calculations of the oxygen-diffusion mechanism in mixed Fe/Ti perovskites for solid-oxide fuel cells. Ceram Int 2019;45:17646–52. https://doi.org/10.1016/j.ceramint.2019.05.330.
[46] Kuhn M, Kim JJ, Bishop SR, Tuller HL. Oxygen nonstoichiometry and defect chemistry of perovskite-structured BaxSr1-xTi1-yFeyO 3-y/2+δ solid solutions. Chem Mater 2013;25:2970–5. https://doi.org/10.1021/cm400546z.
[47] Ferreira AAL, Abrantes JCC, Jurado JR, Frade JR. Oxygen stoichiometry of Sr0.97(Ti,Fe)O3-δ materials. Solid State Ionics 2000;135:761–4. https://doi.org/10.1016/S0167-2738(00)00375-1.
[48] Yaremchenko AA, Macías J, Kovalevsky AV, Arias-Serrano BI, Frade JR. Electrical conductivity and thermal expansion of Ln-substituted SrTiO3 for solid oxide cell electrodes and interconnects: the effect of rare-earth cation size. J Power Sources 2020;474:228531. https://doi.org/10.1016/j.jpowsour.2020.228531.
[49] Qin M, Gao F, Cizek J, Yang S, Fan X, Zhao L, Xu J, Dong G, Reece M, Yan H. Point defect structure of La-doped SrTiO3 ceramics with colossal permittivity. Acta Mater 2019;164:76–89. https://doi.org/10.1016/j.actamat.2018.10.025.
[50] Jiang SP. Development of lanthanum strontium cobalt ferrite perovskite electrodes of solid oxide fuel cells – a review. Int J Hydrogen Energy 2019;44:7448–93. https://doi.org/10.1016/j.ijhydene.2019.01.212.
[51] Kovalevsky AV, Aguirre MH, Populoh S, Patrício SG, Ferreira NM, Mikhalev SM, Fagg DP, Weidenkaff A, Frade JR. Designing strontium titanate-based thermoelectrics: insight into defect chemistry mechanisms. J Mater Chem A 2017;5:3909–22. https://doi.org/10.1039/c6ta09860f.
[52] Levin I, Krayzman V, Playford HY, Woicik JC, Maier RA, Lu Z, Bruma A, Eremenko M, Tucker MG. The mediation of bond strain by vacancies and displacive disorder in A-site-deficient perovskites. Acta Mater 2021;207. https://doi.org/10.1016/j.actamat.2021.116678.
[53] Li X, Zhao H, Liang J, Luo Y, Chen G, Shi X, Lu S, Gao S, Hu J, Liu Q, Sun X. A-site perovskite oxides: an emerging functional material for electrocatalysis and photocatalysis. J Mater Chem 2021:6650–70. https://doi.org/10.1039/d0ta09756j.
[54] Liang M, Zhu Y, Song Y, Guan D, Luo Z, Yang G, Jiang SP, Zhou W, Ran R, Shao Z. A new durable surface nanoparticles-modified perovskite cathode for protonic ceramic fuel cells from selective cation exsolution under oxidizing atmosphere. Adv Mater 2022;34:1–9. https://doi.org/10.1002/adma.202106379.
[55] Ni W, Zhu T, Chen X, Zhong Q, Ma W. Stable, efficient and cost-competitive Ni-substituted Sr(Ti,Fe)O3 cathode for solid oxide fuel cell: effect of A-site deficiency. J Power Sources 2020;451:227762. https://doi.org/10.1016/j.jpowsour.2020.227762.
[56] Ni W, Ma W, Zhong Q, Zhu T, Han M. Synthesis and electrochemical performance of Ni substituted SrTi0.3Fe0.7O3-δ cathode: effect of A-site deficiency. ECS Trans 2019;91:1535–41.
[57] Shan K, Guo XM. Electrical properties of (Y0.08Sr0.92)1-xTi0.6Fe0.4O3-δ mixed conductor. Electrochim Acta 2015;154:31–4. https://doi.org/10.1016/j.electacta.2014.12.057.
[58] Kharton VV, Kovalevsky AV, Tsipis EV, Viskup AP, Naumovich EN, Jurado JR, Frade JR. Mixed conductivity and stability of A-site-deficient Sr(Fe,Ti)O 3-δ perovskites. J Solid State Electrochem 2003;7:30–6. https://doi.org/10.1007/s10008-002-0286-3.
[59] Yang H, Hanif MB, Zhang SL, Li CJ, Li CX. Sintering behavior and electrochemical performance of A-site deficient SrxTi0.3Fe0·7O3-δ oxygen electrodes for solid oxide electrochemical cells. Ceram Int 2021;47:25051–8. https://doi.org/10.1016/j.ceramint.2021.05.235.
[60] Li R, Liu F, Zhang C, Liu J, Zhou J, Xu L. Electrical properties of Fe-doped SrTiO3 with B-site-deficient for SOFC anodes. Ceram Int 2019;45:21684–7. https://doi.org/10.1016/j.ceramint.2019.07.167.
[61] Mroziński A, Molin S, Jasiński P. Study of oxygen electrode reactions on symmetrical porous SrTi0.30Fe0.70O3-δ electrodes on Ce0.8Gd0.2O1.9 electrolyte at 800 °C–500 °C. Electrochim Acta 2020;346:136285. https://doi.org/10.1016/j.electacta.2020.136285.
[62] Mroziński A, Molin S, Jasiński P. Effect of sintering temperature on electrochemical performance of porous SrTi1-xFexO3-δ (x = 0.35, 0.5, 0.7) oxygen electrodes for solid oxide cells. J Solid State Electrochem 2020;24:873–82. https://doi.org/10.1007/s10008-020-04534-0.
[63] Li Y, Gerdes K, Horita T, Liu X. Surface exchange and bulk diffusivity of LSCF as SOFC cathode: electrical conductivity relaxation and isotope exchange characterizations. J Electrochem Soc 2013;160:F343. https://doi.org/10.1149/2.044304jes. –F350.
[64] Ciucci F. Electrical conductivity relaxation measurements: statistical investigations using sensitivity analysis, optimal experimental design and ECRTOOLS. Solid State Ionics 2013;239:28–40. https://doi.org/10.1016/j.ssi.2013.03.020.
[65] Wan TH, Saccoccio M, Chen C, Ciucci F. Influence of the discretization methods on the distribution of relaxation times deconvolution: implementing radial basis functions with DRTtools. Electrochim Acta 2015;184:483–99. https://doi.org/10.1016/j.electacta.2015.09.097.
[66] Staykov A, Fukumori S, Yoshizawa K, Sato K, Ishihara T, Kilner J. Interaction of SrO-terminated SrTiO3 surface with oxygen, carbon dioxide, and water. J Mater Chem A 2018;6:22662–72. https://doi.org/10.1039/c8ta05177a.
[67] Rhodes NR, Barde A, Randhir K, Li L, Hahn DW, Mei R, Klausner JF, Auyeung N. Solar thermochemical energy storage through carbonation cycles of SrCO3/SrO supported on SrZrO3. ChemSusChem 2015;8:3793–8. https://doi.org/10.1002/cssc.201501023.
[68] Bagherisereshki E, Tran J, Lei F, AuYeung N. Investigation into SrO/SrCO3 for high temperature thermochemical energy storage. Sol Energy 2018;160:85–93. https://doi.org/10.1016/j.solener.2017.11.073.
[69] Mizera A, Kowalczyk A, Chmielarz L, Drożdż E. Catalysts based on strontium titanate doped with Ni/Co/Cu for dry reforming of methane. Materials 2021;14. https://doi.org/10.3390/ma14237227.

[70] Miruszewski T, Dzierzgowski K, Winiarz P, Wachowski SL, Mielewczyk–Gryń A, Gazda M. Structural properties and water uptake of SrTi1-xFexO3-x/2-δ. Materials 2020;13:1–16. https://doi.org/10.3390/ma13040965.
[71] Zhao H, Gao F, Li X, Zhang C, Zhao Y. Electrical properties of yttrium doped strontium titanate with A-site deficiency as potential anode materials for solid oxide fuel cells. Solid State Ionics 2009;180:193–7. https://doi.org/10.1016/j.ssi.2008.11.018.
[72] Shannon RD. Revised effective ionic radii and systematic studies of interatomic distances in halides and chalcogenides. Acta Crystallogr A 1976;32:751–67. https://doi.org/10.1107/S0567739476001551.
[73] Ward S, Isaacs MA, Gupta G, Mamlouk M, Pramana SS. Boosting the oxygen evolution activity in non-stoichiometric praseodymium ferrite-based perovskites by A site substitution for alkaline electrolyser anodes. Sustain Energy Fuels 2021;5:154–65. https://doi.org/10.1039/d0se01278e.
[74] Schulze-Küppers F, Ten Donkelaar SFP, Baumann S, Prigorodov P, Sohn YJ, Bouwmeester HJM, Meulenberg WA, Guillon O. Structural and functional properties of SrTi1-xFexO3-δ ($0 \leq x \leq 1$) for the use as oxygen transport membrane. Sep Purif Technol 2015;147:414–21. https://doi.org/10.1016/j.seppur.2014.12.020.
[75] Tietz F. Thermal expansion of SOFC materials. Ionics 1999;5:129–39. https://doi.org/10.1007/BF02375916.
[76] Løken A, Ricote S, Wachowski S. Thermal and chemical expansion in proton ceramic electrolytes and compatible electrodes. Crystals 2018;8:365. https://doi.org/10.3390/cryst8090365.
[77] Zaza F, Frangini S, Leoncini J, Luisetto I, Masci A, Pasquali M, Tuti S. Temperature-independent sensors based on perovskite-type oxides. AIP Conf Proc 2014;1603:53–61. https://doi.org/10.1063/1.4883042.
[78] Zhang X, Li H, Li Y, Shen W. Structural properties and catalytic activity of Sr-substituted LaFeO3 perovskite. Cuihua Xuebao/Chinese J. Catal. 2012;33:1109–14. https://doi.org/10.1016/S1872-2067(11)60388-4.
[79] Biesinger MC, Payne BP, Grosvenor AP, Lau LWM, Gerson AR, Smart RSC. Resolving surface chemical states in XPS analysis of first row transition metals, oxides and hydroxides: Cr, Mn, Fe, Co and Ni. Appl Surf Sci 2011;257:2717–30. https://doi.org/10.1016/j.apsusc.2010.10.051.
[80] Link C, Opitz AK, Rameshan C, Kubicek M, Rupp GM, Nenning A. The chemical evolution of the - La0.6Sr0.4CoO3–δ surface under SOFC operating conditions and its implications for electrochemical oxygen exchange activity. Top Catal 2019;61:2129–41. https://doi.org/10.1007/s11244-018-1068-1.
[81] Chen Y, Jung W, Cai Z, Kim JJ, Tuller HL, Yildiz B. Impact of Sr segregation on the electronic structure and oxygen reduction activity of SrTi1-xFexO3 surfaces. Energy Environ Sci 2012;5:7979–88. https://doi.org/10.1039/c2ee21463f.
[82] Murakami R, Tanaka H, Shinotsuka H, Nagata K, Shouno H, Yoshikawa H. Development of multiple core-level XPS spectra decomposition method based on the Bayesian information criterion. J Electron Spectrosc Relat Phenom 2020;245:147003. https://doi.org/10.1016/j.elspec.2020.147003.
[83] Nenning A, Opitz AK, Rameshan C, Rameshan R, Blume R, Hävecker M, Knop-Gericke A, Rupprechter G, Klötzer B, Fleig J. Ambient pressure XPS study of mixed conducting perovskite-type SOFC cathode and anode materials under well-defined electrochemical polarization. J Phys Chem C 2016;120:1461–71. https://doi.org/10.1021/acs.jpcc.5b08596.
[84] Merkle R, Maier J. Oxygen incorporation into Fe-doped SrTiO3: mechanistic interpretation of the surface reaction. Phys Chem Chem Phys 2002;4:4140–8. https://doi.org/10.1039/b204032h.
[85] Goel V, Cox D, Barnett SA, Thornton K. Simulation of the electrochemical impedance in a three-dimensional, complex microstructure of solid oxide fuel cell cathode and its application in the microstructure characterization. Front Chem 2021;9:1–14. https://doi.org/10.3389/fchem.2021.627699.
[86] Merkle R, Maier J. How is oxygen incorporated into oxides? A comprehensive kinetic study of a simple solid-state reaction with SrTiO3 as a model material. Angew Chem Int Ed 2008;47:3874–94. https://doi.org/10.1002/anie.200700987.
[87] Siebenhofer M, Huber T, Artner W, Fleig J, Kubicek M. Substrate stoichiometry changes during pulsed laser deposition: a case study on SrTiO3. Acta Mater 2021;203. https://doi.org/10.1016/j.actamat.2020.10.077.
[88] Steele BCH. Survey of materials selection for ceramic fuel cells. Solid State Ionics 1996;88:1223–34.
[89] Md Harashid MA, Chen RS, Ahmad SH, Ismail AF, Baharuddin NA. Recent advances in electrode material for symmetrical solid oxide fuel cells and way forward sustainability based on local mineral resources. Int J Energy Res 2022;46:22188–221. https://doi.org/10.1002/er.8579.
[90] Muhammed Ali SA, Anwar M, Baharuddin NA, Somalu MR, Muchtar A. Enhanced electrochemical performance of LSCF cathode through selection of optimum fabrication parameters. J Solid State Electrochem 2018;22:263–73. https://doi.org/10.1007/s10008-017-3754-5.
[91] Jung W, Tuller HL. Investigation of cathode behavior of model thin-film SrTi[sub 1–x]Fe[sub x]O[sub 3–δ] (x=0.35 and 0.5) mixed ionic-electronic conducting electrodes. J Electrochem Soc 2008;155:B1194. https://doi.org/10.1149/1.2976212. –B1201.
[92] Jung W, Tuller HL. Impedance study of SrTi1-xFexO3-δ (x = 0.05 to 0.80) mixed ionic-electronic conducting model cathode. Solid State Ionics 2009;180:843–7. https://doi.org/10.1016/j.ssi.2009.02.008.
[93] Escudero MJ, Aguadero A, Alonso JA, Daza L. A kinetic study of oxygen reduction reaction on La2NiO4 cathodes by means of impedance spectroscopy. J Electroanal Chem 2007;611:107–16. https://doi.org/10.1016/j.jelechem.2007.08.006.
[94] Mroziński A, Błaszczak P, Górnicka K, Miruszewski T, Karczewski J, Molin S, Jasiński P. Impact of strontium non-stoichiometry of SrxTi0.3Fe0, 7O3-δ; 2022. https://doi.org/10.34808/yhx3-f485.